Article

Revitalizing interface in protonic ceramic cells by acid etch

https://doi.org/10.1038/s41586-022-04457-y

Received: 26 May 2021

Accepted: 24 January 2022

Published online: 20 April 2022

Check for updates

Wenjuan Bian[1,2,6], Wei Wu[1,6]✉, Baoming Wang[3], Wei Tang[1,2], Meng Zhou[2], Congrui Jin[4], Hanping Ding[1], Weiwei Fan[5], Yanhao Dong[5]✉, Ju Li[3,5]✉ & Dong Ding[1]✉

Protonic ceramic electrochemical cells hold promise for operation below 600 °C (refs. [1,2]). Although the high proton conductivity of the bulk electrolyte has been demonstrated, it cannot be fully used in electrochemical full cells because of unknown causes[3]. Here we show that these problems arise from poor contacts between the low-temperature processed oxygen electrode–electrolyte interface. We demonstrate that a simple acid treatment can effectively rejuvenate the high-temperature annealed electrolyte surface, resulting in reactive bonding between the oxygen electrode and the electrolyte and improved electrochemical performance and stability. This enables exceptional protonic ceramic fuel-cell performance down to 350 °C, with peak power densities of 1.6 W cm^{-2} at 600 °C, 650 mW cm^{-2} at 450 °C and 300 mW cm^{-2} at 350 °C, as well as stable electrolysis operations with current densities above 3.9 A cm^{-2} at 1.4 V and 600 °C. Our work highlights the critical role of interfacial engineering in ceramic electrochemical devices and offers new understanding and practices for sustainable energy infrastructures.

Protonic ceramic fuel/electrolysis cells (PCFCs/PCECs) promise intermediate-temperature (400–600 °C) applications for reversible conversions between chemical and electrical energy with high efficiency and zero emissions[1–4]. One of their key components is the perovskite-structure oxide electrolyte (for example, $BaZr_{0.1}Ce_{0.7}Y_{0.1}Yb_{0.1}O_{3-\delta}$ (BZCYYb) and $BaZr_{0.8}Y_{0.2}O_{3-\delta}$ (BZY)), whose high bulk proton conductivity enables lower temperature operations than those for oxygen ion conductor-based solid oxide fuel/electrolysis cells (SOFCs/SOECs) because of smaller activation energy[5–7]. Nevertheless, there are still electrolyte-related challenges that limit PCFC/PCEC applications. First, even though the sintered bulk electrolyte shows high proton conductivity (for example, >10 mS cm^{-1} at 500 °C), the ohmic resistance in electrochemical cells is larger than the theoretical value estimated from bulk ionic conductivity alone, with an 'unidentified origin'. The inconsistency has been proposed to originate from poor contacts between the oxygen electrode and electrolyte[3]. Second, the oxygen electrode–electrolyte interface is mechanically weak, which causes delamination and other forms of degradation, especially under high-current-density PCEC operations.

PCFCs/PCECs are typically prepared by first cosintering the hydrogen electrode–electrolyte bilayer at a high temperature T_1, and then screen-printing or painting the oxygen electrode layer, followed by a second step of sintering at a lower temperature T_2 (Fig. 1a). However, the protonic ceramic electrolytes are difficult to densify, which requires cosintering at $T_1 \geq 1{,}400$ °C for BZCYYb and $T_1 \geq 1{,}500$ °C for BZY[8–10]. These temperatures are much higher than those required to sinter fluorite-structure oxygen ion conductors used in SOFCs/SOECs (T_1 roughly 1,250 °C for gadolinium-doped ceria and roughly 1,300 °C for yttria-stabilized zirconia)[11–13]. This contrast exists despite the fact that $BaCeO_3$ (melting temperature $T_m = 2{,}150$ °C) and $BaZrO_3$ ($T_m = 2{,}700$ °C) have similar T_m to CeO_2 ($T_m = 2{,}400$ °C) and ZrO_2 ($T_m = 2{,}715$ °C), respectively, and Ce and Zr are the rate-limiting elements for mass transport in both perovskite- and fluorite-structure systems[14,15]. Although seemingly unrelated to full-cell performance at 400–600 °C, we propose that the low true contact area and high interfacial impedance have the same origin as the poor sinterability resulting from slow mass transport. In fact, the situation is even worse for T_2 sintering (roughly 1,000 °C): a porous oxygen electrode has to be diffusion-bonded to an already well-annealed electrolyte surface (take constrained sintering on a single crystal substrate as an extreme analogy) and T_2 has to be low enough to avoid coarsening of the porous oxygen electrode to allow gas transport and catalysis. Considering the above, we proposed an acid treatment to rejuvenate the high-temperature annealed electrolyte surface (Fig. 1a) before bonding with the oxygen electrode. We demonstrated that it can fully recover the theoretical bulk proton conductivity in electrochemical cells and significantly improve the cell performance as well as thermomechanical and electrochemical stabilities.

Interfacial rejuvenation

To prepare the hydrogen electrode-supported half cells, a NiO+BZCYYb hydrogen electrode and a BZCYYb electrolyte were cosintered to produce a dense electrolyte with a coarse grain structure (Fig. 1b), a thickness of around 22 μm and a relatively flat surface with a roughness of 0.28 μm (Fig. 1d, by quantitative atomic force microscopy (AFM)). This well-annealed surface impedes the oxygen electrode ($PrNi_{0.5}Co_{0.5}O_{3-\delta}$

[1]Energy and Environmental Science and Technology, Idaho National Laboratory, Idaho Falls, ID, USA. [2]Department of Chemical and Materials Engineering, New Mexico State University, Las Cruces, NM, USA. [3]Department of Materials Science and Engineering, Massachusetts Institute of Technology, Cambridge, MA, USA. [4]Department of Civil and Environmental Engineering, University of Nebraska–Lincoln, Lincoln, NE, USA. [5]Department of Nuclear Science and Engineering, Massachusetts Institute of Technology, Cambridge, MA, USA. [6]These authors contributed equally: Wenjuan Bian, Wei Wu. ✉e-mail: wei.wu@inl.gov; dongyh@mit.edu; liju@mit.edu; dong.ding@inl.gov

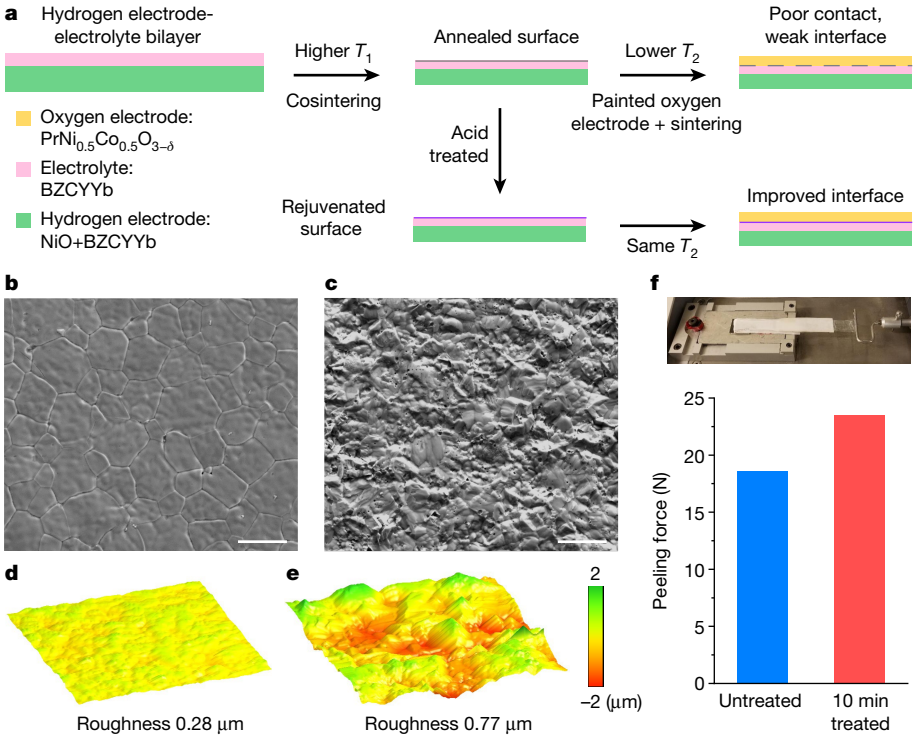

Fig. 1 | Rejuvenated surface improves oxygen electrode–electrolyte interfacial strength. a, Schematic PCFC/PCEC fabrication process. **b**, **c**, Microstructure for untreated (**b**) and 10-min treated (**c**) electrolyte surface of cosintered hydrogen electrode–electrolyte bilayer. Scale bars, 20 μm. **d**, **e**, AFM for the untreated (**d**) and 10-min treated (**e**) electrolyte surface. **f**, Peeling strength of cathode–electrolyte interface (lower panel). Upper panel shows a photograph of peeling strength measurement.

(PNC55)) bonding, and results in a mechanically weak oxygen electrode–electrolyte interface with a peeling strength of 18.6 N (Fig. 1f and Supplementary Table 1). To improve the interfacial bonding, we first treated the electrolyte surface of the cosintered hydrogen electrode–electrolyte bilayer with nitric acid, before bonding with the oxygen electrode (Fig. 1a). The acid etching initiates along the grain boundaries and at specific grains (for 1 min of treatment, Supplementary Fig. 1a) of BZCYYb, indicating heterogeneous surface 'inertness' that should be inversely correlated with hetero-oxide bonding. As the treatment time increases, the etching proceeds more uniformly and creates a rough surface (Fig. 1c and Supplementary Figs. 1b–d and 2). We confirmed that the etch does not affect the phase purity of the bulk BZCYYb electrolyte as shown by X-ray diffraction in Supplementary Fig. 3. For chemical uniformity, we conducted energy dispersive spectroscopy (EDS) mapping on the untreated (Supplementary Fig. 4) and 10-min treated (Supplementary Fig. 5) electrolyte surface. Spatially uniform elemental distributions were confirmed in both samples, and the inferred compositions (Supplementary Tables 2 and 3) agreed well with the bulk composition of BZCYYb. For atomic-scale surface chemistry, we conducted X-ray photoelectron spectroscopy (XPS) analysis on the electrolyte surfaces (Supplementary Fig. 6) and found weakened signals of Ba 3*d*5 and Y 3*d* peaks at the 10-min treated surface compared to the untreated one. The inferred cation compositions (Supplementary Table 4) indicate Y segregation and Ba deficiency at the untreated surface. At the 10-min treated surface, there is no obvious Y segregation, and Ba deficiency becomes more severe. The latter is understandable as the acid may preferentially etch away the more reactive BaO units at the surface and leave it terminated with more B-site cations. These chemical features indicate that although the acid treatment does not alter the composition of the bulk region, it drives the nanometre-scale surface chemistry away from its well-annealed profile, which would benefit atomic-scale diffusion and reaction at the oxygen electrode–electrolyte interface for better hetero-phase diffusional bonding. Indeed, the interface of the sintered full cell became stronger with etching treatment (Supplementary Table 1). A maximum peeling strength of 23.5 N was achieved in the 10-min treated cell (Fig. 1f), which correlates with a maximum surface roughness of 0.77 μm (Fig. 1e and Supplementary Fig. 2).

We conducted aberration-corrected scanning transmission electron microscopy (STEM) and EDS of the 10-min treated and diffusion-bonded sample (Fig. 2). Figure 2a–j shows a sample slice (roughly 100 nm thick) near the oxygen electrode–electrolyte interface. Whereas both PNC55 (fine particles on the top, rich in Pr, Ni, Co, and O) and BZCYYb (dense layer on the bottom, rich in Ba, Zr, Ce, Y, Yb and O) can be clearly observed, there is also some new phase observed in between that is rich in Pr, Ni, Zr, Y, Yb and O, but poor in Co and Ce. To get higher spatial resolution and better statistics, we thinned down another slice from a different location to roughly 20 nm in thickness. As shown in Fig. 2k–t, in addition to PNC55 (at the upper left corner) and BZCYYb (on the bottom), we again observed a new phase, this time rich in Pr, Zr, Y, Yb and O. These observations indicate that active chemical reactions take place at the interface during the T_2 sintering. This represents an interfacial version of reactive sintering, which gives better bonding/adhesion under an enhanced chemical driving force. Rough and well-bonded features (Fig. 2u,v) further evidenced the high-quality oxygen electrode–electrolyte interface.

Decreased R_o and R_p: prefactor versus E_a

For electrochemical performance, we first conducted electrochemical impedance spectroscopy (EIS) at open-circuit voltage (OCV) condition at 400–650 °C, for fuel cells across H_2+3% H_2O for the hydrogen electrode and O_2 for the oxygen electrode. As shown in Fig. 3a (at 600 °C; more data at other temperatures are shown in Supplementary Fig. 7), the acid treatment up to 10 min lowers both the ohmic resistance R_o and polarization resistance R_p, whereas the 15-min treatment

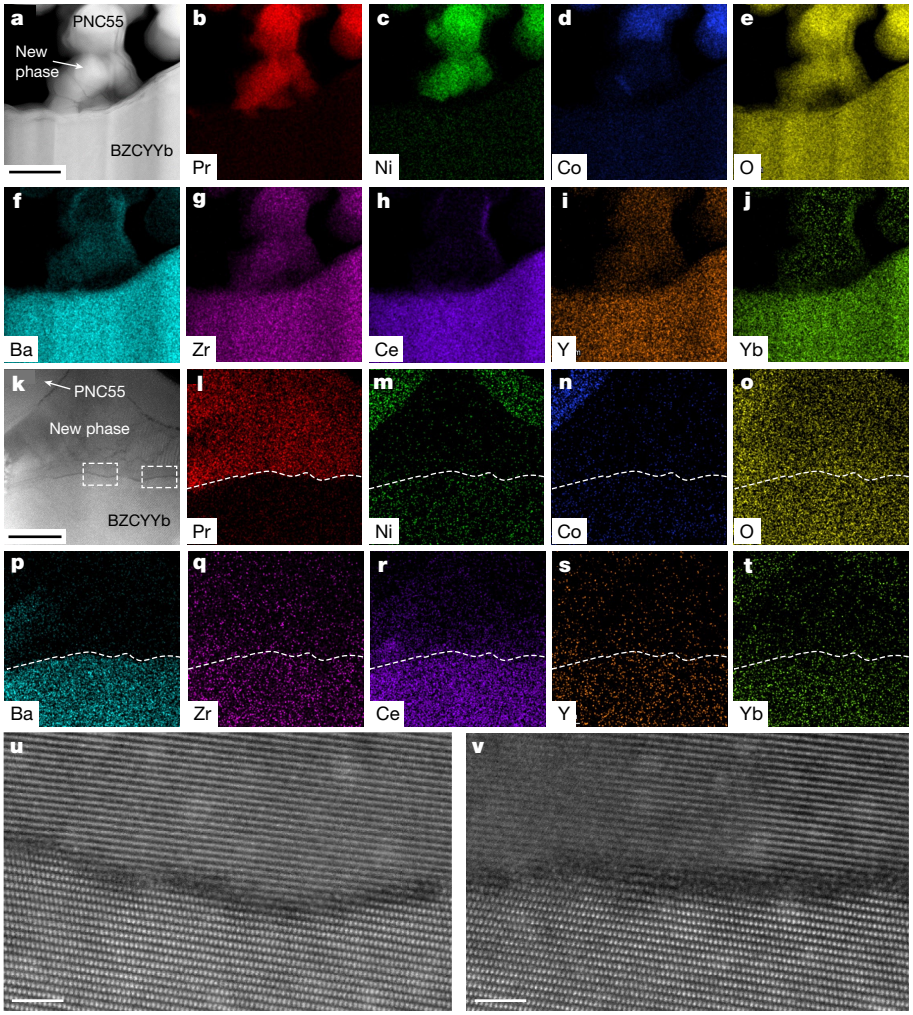

Fig. 2 | Reactive sintering at oxygen electrode–electrolyte interface improves interfacial bonding. a–j, High-angle annular dark-field (HAADF)–STEM image (**a**) of a sample slice near the oxygen electrode–electrolyte interface and the corresponding EDS mapping of Pr (**b**), Ni (**c**), Co (**d**), O (**e**), Ba (**f**), Zr (**g**), Ce (**h**), Y (**i**) and Yb (**j**). **k–t**, HAADF–STEM image (**k**) of a thinned sample slice at another region near the interface and the corresponding EDS mapping of Pr (**l**), Ni (**m**), Co (**n**), O (**o**), Ba (**p**), Zr (**q**), Ce (**r**), Y (**s**) and Yb (**t**). **u**, **v**, High-resolution HAADF–STEM of the two regions marked in **k** (left dashed box (**u**) and right dashed box (**v**)), showing a rough and well-bonded interface. Scale bars, 200 nm (**a**); 40 nm (**k**) and 2 nm (**u**,**v**).

increases R_o and R_p apparently due to over-etching. Here, R_o and R_p are assumed to follow an Arrhenius-type temperature dependence

$$R_o = A_o \exp\left(-\frac{E_{a,o}}{k_B T}\right) \quad (1)$$

$$R_p = A_p \exp\left(-\frac{E_{a,p}}{k_B T}\right) \quad (2)$$

where A is the respective pre-exponent term; E_a is the activation energy; the subscripts o and p denote the ohmic and polarization resistances, respectively; k_B is the Boltzmann constant and T is the absolute temperature. When plotting logR_o versus $1/T$ in Fig. 3b, we found that the curves of differently treated cells were all parallel to each other, and the same also holds for R_p in Fig. 3c. This means that the treatment does not affect the activation energy of R_o and R_p (similar activation energy of $E_{a,o} = 0.358 \pm 0.001$ eV for R_o and $E_{a,p} = 0.903 \pm 0.003$ eV for R_p are deduced for differently treated cells; Fig. 3d, fitting details shown in Supplementary Table 5). Instead, it modifies R_o and R_p by changing only A_o and A_p. This is distinct from the practice of enhancing the kinetics by lowering the activation energy. If one calculates the enhancement factor for $1/A_o$ and $1/A_p$ in differently treated cells over the $1/A_o^0$ and $1/A_p^0$ in the untreated cell, the data are all close to the line with a slope of unity in A_o^0/A_o versus A_p^0/A_p plot in Fig. 3e. This further allows us to normalize using a dimensionless reduced temperature k_BT/E_a and a dimensionless relative 'resistance' R, and collapse all the data into a single curve in the Arrhenius plot shown in Fig. 3f (see the details in Supplementary Fig. 8). It indicates a single mechanism responsible for the simultaneously lowered R_o and R_p, and it works by lowering their pre-exponential factor without changing the mechanisms of electrode reactions and proton conduction (inferred by unchanged activation energy). Very probably, this is because of the increased true contact area between the oxygen electrode and the electrolyte.

Full-cell performance

The lowered cell resistance enhances full-cell performance for PCEC and PCFC operations. In PCEC, the feedstocks are pure H_2 for the hydrogen electrode and O_2+30% H_2O for the oxygen electrode. When a voltage larger than OCV (for example, 1.04 V at 600 °C) is applied, the absolute value of the current density j (defined as being negative in PCEC and positive in PCFC) characterizes the cell performance. As shown in Fig. 4a, at the same applied voltage, larger $|j|$ is achieved in treated cells

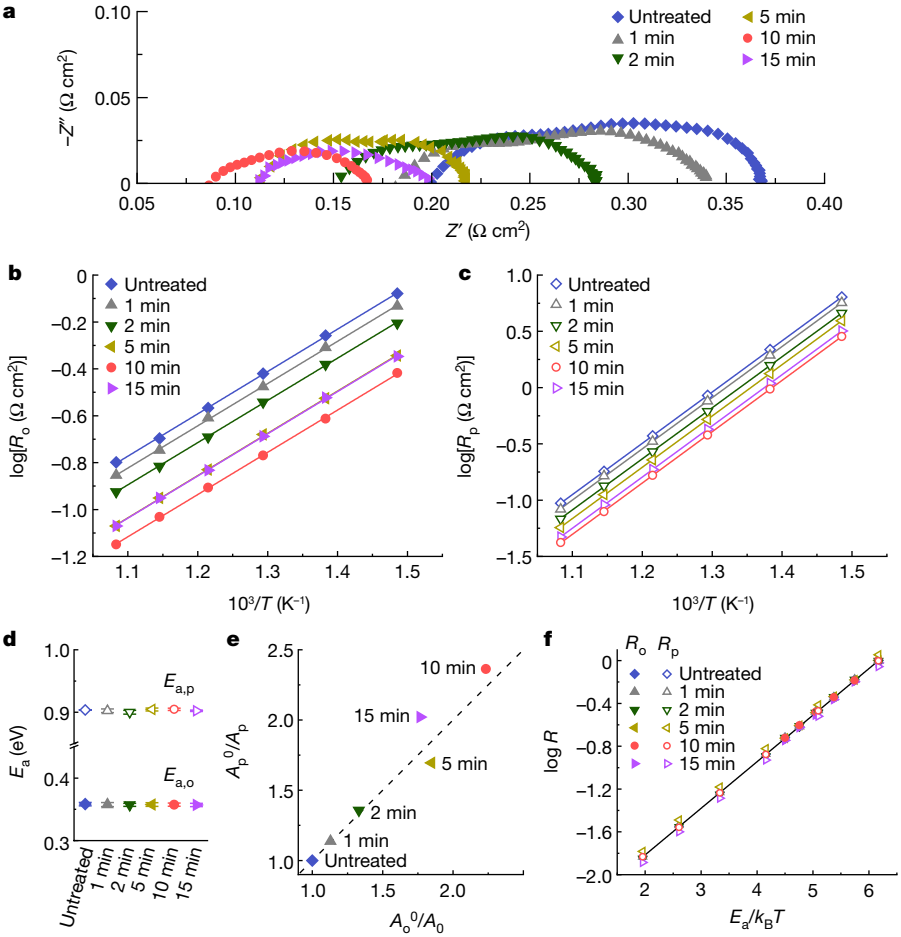

Fig. 3 | Correlation between simultaneously lowered ohmic and polarization resistance. a, EIS at OCV at 600 °C. Z' and Z'' denote the real and imaginary parts of the complex impedance, respectively. R_o is taken from left intercept of the EIS curve with x axis and R_p is taken from right intercept of the EIS curve with x axis minus R_o. **b**, **c**, Arrhenius plot of ohmic (**b**) and polarization (**c**) resistance for differently treated cells. **d**, Calculated activation energy. **e**, Correlation between enhanced kinetics A_o^0/A_o versus A_p^0/A_p. The dashed line with a slope of unity is shown as a guide to the eye. **f**, Arrhenius plot of relative 'resistance' R against the inverse of reduced temperature k_BT/E_a. Cells made up of 22-μm-thick BZCYYb electrolyte and PNC55 oxygen electrode and with different etching treatment conditions.

than in the untreated ones. A 2.8-fold increase over the untreated cell is demonstrated in the 10-min treated cell at 1.4 V at 600 °C, reaching $|j| = 3.07$ A cm^{-2} for PCEC. In addition, the 10-min treated cell demonstrates higher Faradic efficiency (Supplementary Fig. 9a) and H_2 production rate (Supplementary Fig. 9b) than the untreated cell. In PCFC, the current density (positive) is also higher in treated cells at the same voltage (Fig. 4b). A 2.5-fold increase over the untreated cell in peak power density P_{max} is demonstrated in the 10-min treated cell, reaching $P_{max} = 1.18$ W cm^{-2} at 600 °C. Again, the 10-min treated cell shows the best electrochemical performance among all the cells within the entire range of investigated temperatures (see more data in Supplementary Figs. 10–12).

Notwithstanding the 'standard' electrolyte and electrode compositions and readily processed cell architecture, the 10-min treated cell outperforms the reported PCFC data in the literature (Fig. 4c, filled circles in red), offering P_{max} in the full temperature range for PCFCs[3,16–19], despite the fact that our untreated cell lies on the lower end. We also compared the 'apparent' proton conductivity σ (inferred from ohmic loss of EIS measurements and normalized by the dimension of the electrolyte membrane) of BZCYYb-based electrolyte in electrochemical cells[3,20,21]. As shown in Fig. 4d, σ in the 10-min treated cell (filled circles in red) is not only higher than the literature results, but also fully recovers its intrinsic, theoretical value in bulk BZCYYb samples (reaching roughly 97% of intrinsic conductivity, versus only around 44% in the untreated cell).

Suppressed degradations

We next conducted accelerated degradation tests under high-current-density PCEC operations. At a constant applied voltage of 1.4 V at 600 °C, the 10-min treated PCEC had a high initial j of around −3.24 A cm^{-2} and was stable over 200 h of continuous operation (Supplementary Fig. 13a, with 0.94% decay in $|j|$ in 0–100 h and 0.05% decay in 100–200 h). In comparison, the untreated cell not only had a smaller initial j (−1.35 A cm^{-2}), but also suffered from fast degradation (with 10.2% decay in $|j|$ in 0–100 h and 5.9% decay in 100–200 h). (The cycling performances of the cells treated under other conditions and tested under the same PCEC condition are shown in Supplementary Fig. 14, which are improved over the untreated cells but still worse than the 10-min treated one). Post-testing analysis of the cell (fractured by us for sample preparation, not from electrochemical testing) revealed a severe delamination problem with the oxygen electrode (Supplementary Fig. 13b) in the untreated cell after electrochemical cycling. Meanwhile, there was an obvious change in the fracture mode of the BZCYYb electrolyte layer, from intragranular cracking in the untested cell (Supplementary Fig. 15a) to intergranular cracking. This indicates weakened grain boundary adhesion in the perovskite electrolyte, probably due to the generation of gas bubbles at grain boundaries[22–26]. In comparison, there was no observable oxygen electrode delamination, and BZCYYb retained its intragranular-cracking behaviour in the 10-min treated PCEC after 200 h of testing (Supplementary Fig. 13c;

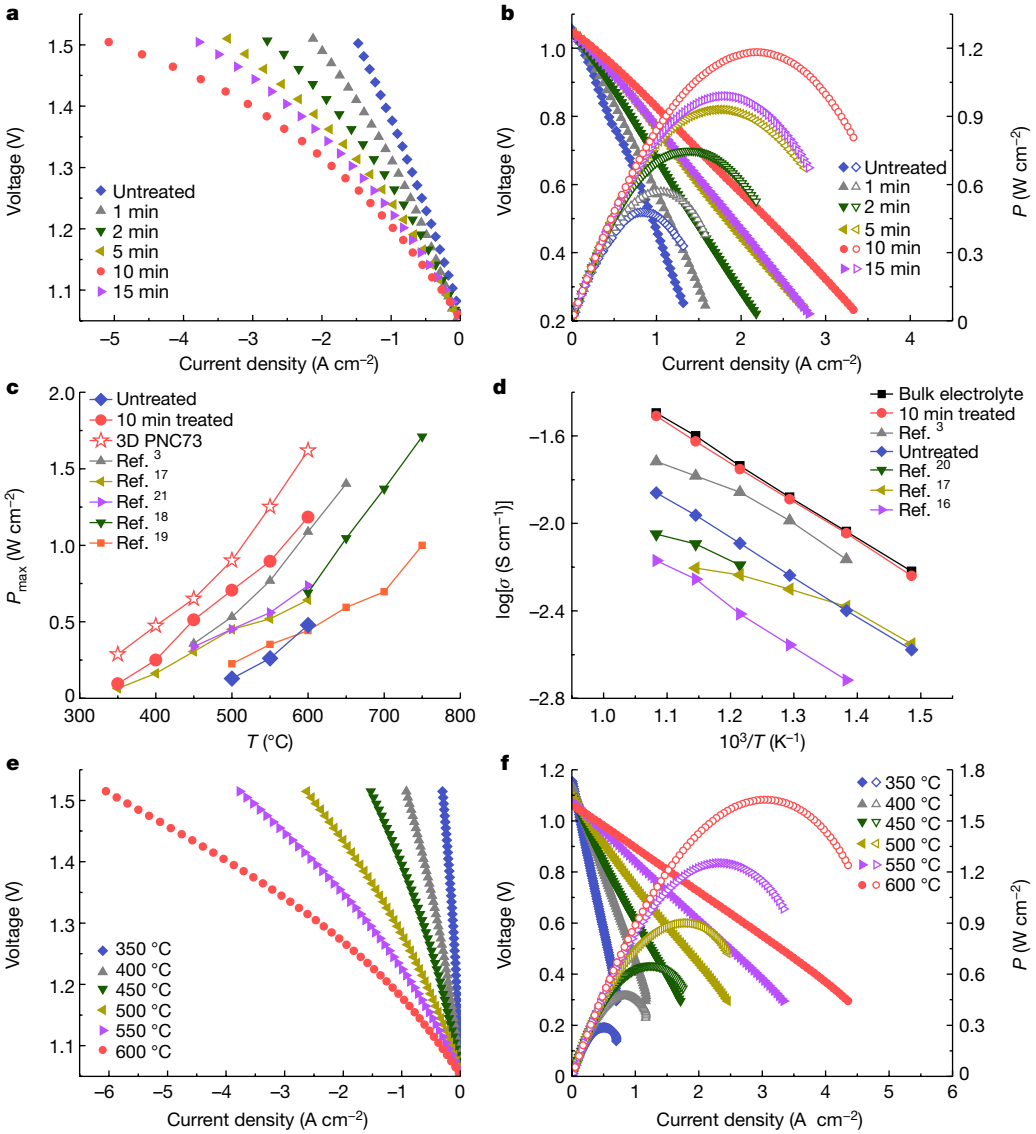

Fig. 4 | Boosted electrochemical performance with modified oxygen electrode–electrolyte interface. a, Polarization curves in PCEC operations at 600 °C. **b**, Polarization and power density curves in PCFC operations at 600 °C. Cells made up of 22-μm-thick BZCYYb electrolyte and PNC55 oxygen electrode and with different etching treatment conditions. Solid and open symbols are for the left *y* axis (voltage) and right *y* axis (power density *P*), respectively. **c**, **d**, Comparison of P_{max} (**c**) and σ (**d**) with literature data[3,16–21]. Dissolved/doped NiO in protonic electrolytes were reported to lower the proton conductivity[10]. This phenomenon is not seen in our BZCYYb electrolyte in full cells, as it fully recovers the bulk value. **e**, **f**, Polarization curves in PCEC operations (**e**), and polarization and power density curves in PCFC operations (**f**) of cells made up of 16-μm-thick BZCYYb electrolyte and 3D PNC73 oxygen electrode and with the 10-min etching treatment before the oxygen electrode was attached. P_{max} values obtained in **f** are plotted as open stars in red in **c** for comparison.

same as the untested cell, Supplementary Fig. 15b). EIS measurements (Supplementary Fig. 16a and Supplementary Table 6) showed increased R_o and R_p values for the untreated cell after PCEC testing, whereas R_o and R_p were similar for the 10-min treated cell before and after testing. The polarization curves (Supplementary Fig. 16b) further confirm the stable PCEC performance of the 10-min treated cell, whereas the untreated one showed lower initial performance and faster degradation. Therefore, we conclude that the treatment consistently improves the electrochemical, mechanical and microstructural stabilities because of better interfacial bonding and higher electrochemical activity (lower overpotential in operation).

Optimizations towards lower *T* operations

We generalized our findings to other interfaces and optimized the full cells to achieve improved performance at lower operating temperatures. On the electrolyte side, we decreased the thickness of BZCYYb from 22 to 16 μm. On the oxygen electrode side, in addition to PNC55, we synthesized the state-of-the-art candidates of $La_{0.6}Sr_{0.4}Co_{0.2}Fe_{0.8}O_{3-\delta}$ (LSCF) and $PrBa_{0.5}Sr_{0.5}Co_{1.5}Fe_{0.5}O_{5+\delta}$ (PBSCF), explored the compositional space of $PrNi_xCo_{1-x}O_{3-\delta}$ ($0 < x < 1$) to obtain $PrNi_{0.7}Co_{0.3}O_{3-\delta}$ (PNC73) with the best performance and engineered the porous electrode microstructure to obtain a three-dimensional $PrNi_{0.7}Co_{0.3}O_{3-\delta}$ mesh (3D PNC73). These materials were tested in full cells (their microstructures are shown in Supplementary Fig. 17) under PCFC (Supplementary Fig. 18) and PCEC operations (Supplementary Fig. 19) at 600 °C with and without 10 min of acid etching treatment. Our data demonstrate that the treatment effectively improved the cell performance in all cases, increasing the PCFC peak power density by roughly 65–180% (Supplementary Fig. 20a; data at other temperatures are summarized in Supplementary Table 7) and the PCEC current density by 60–200% (Supplementary Fig. 20b) at 1.4 V of applied voltage. We confirmed the full-cell reliability

by conducting leakage tests (Supplementary Fig. 21), evaluating fuel flexibility (using CH_4 and C_2H_6, Supplementary Fig. 22), fuel efficiencies (>98% for all measured cells, Supplementary Table 8), and PCFC stability (0.07% decay over 200 h of continuous operation at 0.75 V at 600 °C for the 10-min treated cell using the PNC73 oxygen electrode, Supplementary Fig. 23). The protonic full cell made of 16 μm of BZCYYb electrolyte and a 3D PNC73 oxygen electrode under 10 min of treatment showed exceptional PCFC and PCEC performance (Fig. 4e, f), offering a peak power density of roughly 1,600 mW cm^{-2} at 600 °C, 1,250 mW cm^{-2} at 550 °C, 900 mW cm^{-2} at 500 °C, 650 mW cm^{-2} at 450 °C, 470 mW cm^{-2} at 400 °C and 290 mW cm^{-2} at 350 °C (open stars in red in Fig. 4c). This represents a major step in the practical use of ceramic fuel cells from 600 down to 350 °C, which highlights the critical role of interfacial engineering in 'all-solid-state' electrochemical devices.

Discussion

The coupled electrochemomechanics at the electrode–electrolyte interface affects the thermomechanical integrity, microstructural stability, electrochemical performance and durability of ceramic electrochemical cells. Although much attention has been paid to developing better catalysts and new architecture of the active electrode, our work highlights the equal importance of properly integrating them with the solid electrolyte so that their 'intrinsic' performance can be fully used in full cells. The mechanistic study shows that the proposed acid treatment recovers not only the intrinsic bulk proton conductivity of the electrolyte in full cells (in light of the decreased ohmic resistance), but also the high activity of the BZCYYb/PNC55/gas triple-phase boundary in light of the decreased R_p. In a previous report[3], the former was partially recovered by a 100-nm-thick dense PBSCF interlayer (which is a mixed ionic–electronic conductor and fabricated by pulsed laser deposition) between the porous oxygen electrode (PBSCF) and the electrolyte ($BaZr_{0.4}Ce_{0.4}Y_{0.1}Yb_{0.1}O_{3-\delta}$). Yet, the polarization resistance remained unchanged, which is different from the present study for the PNC55 model system. We believe the difference lies in the mechanism of the oxygen electrode half reaction. In the case of the PBSCF electrode, the half reaction primarily takes place at the PBSCF–gas double-phase boundary, as demonstrated by dimensional analysis in ref. [3]. Furthermore, with the pulsed-laser-deposited dense interlayer, there is no triple-phase boundary, as the electrolyte is not in direct contact with the inlet gas of the oxygen electrode. In the case of PNC55, the fact that R_o and R_p can be simultaneously decreased with similar ratios demonstrates that the half reaction primarily takes place near the triple-phase boundary, given the somewhat lower proton conductivity in PNC55 compared to BZCYYb. It further indicates that the mixed-conductive PNC55 may also have a weaker proton conductivity than PBSCF, and thus its activity in full cells is more critically dependent on the oxygen electrode–electrolyte interface. This offers a plausible explanation for the lowered ohmic loss by interfacial modification: for the untreated cell, PNC55 has poor bonding and a limited contact area with the BZCYYb electrolyte (Supplementary Fig. 24a). As a result, there are not enough reaction sites near the oxygen electrode–electrolyte interface, and a large portion of the interfacial reactions may need to happen at the surface of PNC55 particles relatively far away from the interface, enabled by proton conduction in the PNC55 lattice. Such proton conduction in PNC55 would contribute to the ohmic loss of the full cell. In contrast, with the proper acid treatment, PNC55 now has good bonding and abundant contacts with the BZCYYb electrolyte (Supplementary Fig. 24b). This means that there are sufficient reaction sites near the interface, and no extended proton conduction in PNC55 is required. Therefore, the intrinsic bulk proton conductivity can be achieved in full cells.

Regarding the improved interfacial bonding, there is an apparent contribution from the surface roughness. To mimic such a physical effect, we used sandpapers to mechanically polish the electrolyte surface before bonding the oxygen electrode. Although polishing does increase the surface roughness (Supplementary Figs. 25 and 26), we found that coarse-grit sandpapers can easily damage the electrolytes and cause gas leakage (Supplementary Fig. 27); fine-grit sandpaper polishing only offers marginal performance benefits compared to the untreated cell, which is still much worse than the acid-treated one (Supplementary Fig. 28). This demonstrates pronounced chemical rejuvenation effects in the acid treatment assisted interfacial bonding, in the removal of segregating elements and reactive sintering. The acid treatment is a simple and generic approach, and we believe it can be combined with other materials and architectures to enable more efficient and robust protonic ceramic devices.

Conclusions

To summarize, we demonstrated that a simple acid treatment, which is completely compatible with the state-of-the-art multilayer processing technique of ceramic fuel or electrolysis cells, can rejuvenate the high-temperature annealed electrolyte surface, improve hetero-oxide bonding and recover the intrinsic conductivity and activity of the components for maximum performance. The underlying mechanism is revealed, and the 'unidentified origin' of residual ohmic losses is now understood. The scientific understanding, the practical solution and the applicability to various interfaces provided here can help the rapid insertion of protonic ceramic electrochemical cells into the sustainable energy infrastructure, such as nuclear heat- and electricity-driven production of chemical fuels for seasonal energy storage, and CO_2 capture and use, in an electrical grid strongly influenced by intermittent solar and wind generation. Beyond ceramic fuel cells, interfacial engineering and specially designed processing techniques are also critical to other electrochemical materials and devices, such as oxide cathodes of lithium-ion batteries[27–29], all-solid-state batteries[30] and metal–ceramic interfaces.

Online content

Any methods, additional references, Nature Research reporting summaries, source data, extended data, supplementary information, acknowledgements, peer review information; details of author contributions and competing interests; and statements of data and code availability are available at https://doi.org/10.1038/s41586-022-04457-y.

1. Ding, H. et al. Self-sustainable protonic ceramic electrochemical cells using a triple conducting electrode for hydrogen and power production. *Nat. Commun.* **11**, 1907 (2020).
2. Li, M. et al. Switching of metal–oxygen hybridization for selective CO_2 electrohydrogenation under mild temperature and pressure. *Nat. Catal.* **4**, 274–283 (2021).
3. Choi, S. et al. Exceptional power density and stability at intermediate temperatures in protonic ceramic fuel cells. *Nat. Energy* **3**, 202–210 (2018).
4. Duan, C. et al. Highly efficient reversible protonic ceramic electrochemical cells for power generation and fuel production. *Nat. Energy* **4**, 230–240 (2019).
5. Yang, L. et al. Enhanced sulfur and coking tolerance of a mixed ion conductor for SOFCs: $BaZr_{0.1}Ce_{0.7}Y_{0.2-x}Yb_xO_{3-\delta}$. *Science* **326**, 126–129 (2009).
6. Fabbri, E., Bi, L., Pergolesi, D. & Traversa, E. Towards the next generation of solid oxide fuel cells operating below 600 °C with chemically stable proton-conducting electrolytes. *Adv. Mater.* **24**, 195–208 (2012).
7. Rashid, N. L. R. M. et al. Review on zirconate-cerate-based electrolytes for proton-conducting solid oxide fuel cell. *Ceram. Int.* **45**, 6605–6615 (2019).
8. Peng, C., Melnik, J., Luo, J.-L., Sanger, A. R. & Chuang, K. T. $BaZr_{0.8}Y_{0.2}O_{3-\delta}$ electrolyte with and without ZnO sintering aid: preparation and characterization. *Solid State Ion.* **181**, 1372–1377 (2010).
9. Shimada, H. et al. Effect of Ni diffusion into $BaZr_{0.1}Ce_{0.7}Y_{0.1}Yb_{0.1}O_{3-\delta}$ electrolyte during high temperature co-sintering in anode-supported solid oxide fuel cells. *Ceram. Int.* **44**, 3134–3140 (2018).
10. Okuyama, Y., Ebihara, N., Okuyama, K. & Mizutani, Y. Improvement of protonic ceramic fuel cells with thin film BCZY electrolyte. *ECS Trans.* **68**, 2545 (2015).
11. Arabacı, A. & Öksüzömer, M. F. Preparation and characterization of 10 mol% Gd doped CeO_2 (GDC) electrolyte for SOFC applications. *Ceram. Int.* **38**, 6509–6515 (2012).
12. Zhang, S.-L., Chen, K., Zhang, A.-P., Li, C.-X. & Li, C.-J. Effect of Fe doping on the performance of suspension plasma-sprayed $PrBa_{0.5}Sr_{0.5}Co_{2-x}Fe_xO_{5+\delta}$ cathodes for intermediate-temperature solid oxide fuel cells. *Ceram. Int.* **43**, 11648–11655 (2017).
13. Zha, S., Moore, A., Abernathy, H. & Liu, M. GDC-based low-temperature SOFCs powered by hydrocarbon fuels. *J. Electrochem. Soc.* **151**, A1128 (2004).
14. Melekh, B.-T. et al. Structure, phase transitions and optical properties of pure and rare earth doped $BaCeO_3$, $SrCeO_3$ prepared by inductive melting. *Solid State Ion.* **97**, 465–470 (1997).

15. Yamanaka, S. et al. Thermophysical properties of $BaZrO_3$ and $BaCeO_3$. *J. Alloys Compd.* **359**, 109–113 (2003).
16. An, H. et al. A 5×5 cm^2 protonic ceramic fuel cell with a power density of 1.3 W cm^{-2} at 600 °C. *Nat. Energy* **3**, 870–875 (2018).
17. Duan, C. et al. Readily processed protonic ceramic fuel cells with high performance at low temperatures. *Science* **349**, 1321–1326 (2015).
18. Kim, J. et al. Triple-conducting layered perovskites as cathode materials for proton-conducting solid oxide fuel cells. *Chem. Sus. Chem.* **7**, 2811–2815 (2014).
19. Nguyen, N. T. Q. & Yoon, H. H. Preparation and evaluation of $BaZr_{0.1}Ce_{0.7}Y_{0.1}Yb_{0.1}O_{3-\delta}$ (BZCYYb) electrolyte and BZCYYb-based solid oxide fuel cells. *J. Power Sources* **231**, 213–218 (2013).
20. Song, Y. et al. Self-assembled triple-conducting nanocomposite as a superior protonic ceramic fuel cell cathode. *Joule* **3**, 2842–2853 (2019).
21. Bae, K. et al. Demonstrating the potential of yttrium-doped barium zirconate electrolyte for high-performance fuel cells. *Nat. Commun.* **8**, 14553 (2017).
22. Park, B.-K., Zhang, Q., Voorhees, P. W. & Barnett, S. A. Conditions for stable operation of solid oxide electrolysis cells: oxygen electrode effects. *Energy Environ. Sci.* **12**, 3053–3062 (2019).
23. Laguna-Bercero, M., Campana, R., Larrea, A., Kilner, J. & Orera, V. Electrolyte degradation in anode supported microtubular yttria stabilized zirconia-based solid oxide steam electrolysis cells at high voltages of operation. *J. Power Sources* **196**, 8942–8947 (2011).
24. Graves, C., Ebbesen, S. D., Jensen, S. H., Simonsen, S. B. & Mogensen, M. B. Eliminating degradation in solid oxide electrochemical cells by reversible operation. *Nat. Mater.* **14**, 239–244 (2015).
25. Dong, Y., Zhang, Z., Alvarez, A. & Chen, I.-W. Potential jumps at transport bottlenecks cause instability of nominally ionic solid electrolytes in electrochemical cells. *Acta Mater.* **199**, 264–277 (2020).
26. Dong, Y. et al. Chemical and structural origin of hole states in yttria-stabilized zirconia. *Acta Mater.* **203**, 116487 (2021).
27. Xue, W. et al. Ultra-high-voltage Ni-rich layered cathodes in practical Li metal batteries enabled by a sulfonamide-based electrolyte. *Nat. Energy* **6**, 495–505 (2021).
28. Xu, G.-L. et al. Building ultraconformal protective layers on both secondary and primary particles of layered lithium transition metal oxide cathodes. *Nat. Energy* **4**, 484–494 (2019).
29. Yoon, M. et al. Reactive boride infusion stabilizes Ni-rich cathodes for lithium-ion batteries. *Nat. Energy* **6**, 362–371 (2021).
30. Han, X. et al. Negating interfacial impedance in garnet-based solid-state Li metal batteries. *Nat. Mater.* **16**, 572–579 (2017).

Methods

Materials synthesis

BZCYYb was synthesized by a solid-state reaction method. Stoichiometric amounts of $BaCO_3$ (99.8% purity, Alfa Aesar), ZrO_2 (99% purity, Alfa Aesar), CeO_2 (99.9% purity, Alfa Aesar), Y_2O_3 (99.9% purity, Alfa Aesar) and Yb_2O_3 (99.9% purity, Alfa Aesar) were mixed by ball milling in ethanol for 12 h, followed by drying, grinding and heat treatment at 1,100 °C for 8 h to obtain phase-pure BZCYYb powders. PNC55 was synthesized by a Pechini method. Stoichiometric $Pr(NO_3)_3{\cdot}6H_2O$ (99.9% purity, Alfa Aesar), $Ni(NO_3)_2{\cdot}6H_2O$ (99% purity, Alfa Aesar) and $Co(NO_3)_2{\cdot}6H_2O$ (99% purity, Alfa Aesar) were dissolved in deionized water to prepare an aqueous solution containing 0.05 mol l^{-1} Pr^{3+}, 0.025 mol l^{-1} Ni^{2+} and 0.025 mol l^{-1} Co^{2+}. Next, 0.2 mol l^{-1} glycol (99% purity, ACROS Organics) and 0.1 mol l^{-1} citric acid (99% purity, Alfa Aesar) were added. The prepared solution was heated to 80 °C on a hot plate with continuous stirring until it converted to a gel. The obtained gel was heated to 350 °C, followed with an auto-ignition process to produce a black foamy intermediate product. Final PNC55 powders were obtained by annealing the intermediate product at 1,100 °C for 4 h. LSCF, PBSCF and PNC73 were similarly synthesized by the same Pechini method following their stoichiometries, with additional chemicals $Sr(NO_3)_2$ (99.0% purity, Alfa Aesar), $Ba(NO_3)_2$ (ACROS Organics) and $Fe(NO_3)_3{\cdot}9H_2O$ (99.95% purity, Sigma-Aldrich). 3D PNC73 was fabricated by a template-derived method. Stoichiometric $Pr(NO_3)_3{\cdot}6H_2O$, $Ni(NO_3)_2{\cdot}6H_2O$ and $Co(NO_3)_2{\cdot}6H_2O$ were dissolved in deionized water to prepare a nitrate precursor solution containing 0.05 mol l^{-1} Pr^{3+}, 0.035 mol l^{-1} Ni^{2+} and 0.015 mol l^{-1} Co^{2+}. A piece of fabric textile (Telio) was immersed into the precursor solution for 24 h and then heat treated at 750 °C for 2 h to form the 3D PNC73 mesh.

Cell fabrication

Hydrogen electrode-supported cells were fabricated by a tape-casting process. To prepare green tapes of the hydrogen electrode, NiO and BZCYYb powders were mixed with 6 to 4 weight ratio by ball milling in ethanol and toluene for 24 h. Binder of polyvinyl butyral (Tape Casting Warehouse, Inc.), plasticizer of butyl benzyl phthalate (Tape Casting Warehouse, Inc.) and dispersant of fish oil (Tape Casting Warehouse, Inc.) were next added, followed by ball milling for an additional 24 h to yield the desired slip rheology. Tape casting was performed using a laboratory tape-casting machine. The thickness of the hydrogen electrode green tapes was controlled at roughly 1 mm after drying at 37.8 °C for 4 h. Green tapes of electrolyte were prepared similarly without adding NiO and by controlling the thickness to roughly 0.12 mm (for the 22-μm-thick BZCYYb electrolyte after sintering) or roughly 0.08 mm (for the 16-μm-thick BZCYYb electrolyte after sintering) after drying. Three pieces of hydrogen electrode green tapes and one piece of electrolyte green tape were laminated by a hot press at 70 °C under 4 ton for 5 h. Laminated green tapes were punched with 11-mm (7/16-inch) diameter holes and presintered at 920 °C for 3 h to remove the organics. The cosintering of the hydrogen electrode–electrolyte bilayer was conducted at T_1 = 1,400 °C at 5 h (heating rate 1 °C min^{-1} to 1,000 °C and 2 °C min^{-1} to 1,400 °C), followed by a furnace cooling. To treat the surface, 0.3 ml (0.53 ml cm^{-2}) of concentrated nitric acid (Alfa Aesar) was dropped on the electrolyte surface of the cosintered hydrogen electrode–electrolyte bilayer, left for different times from 1 to 15 min and then washed with deionized water. To fabricate full cells, a slurry of oxygen electrodes was prepared by mixing oxygen electrode powders with ethanol and a texanol-based binder (ESL ElectroScience) by ball milling and then brush-painted on the electrolyte surface of the cosintered hydrogen electrode–electrolyte bilayer. For the 3D PNC73 electrode, the heat-treated mesh was first bonded to electrolyte surface using a thin layer of painted PNC73 slurry. The surface area of oxygen electrode was controlled at roughly 0.178 cm^2. The painted cells were sintered at T_2 = 1,000 °C for 4 h (heating rate 3 °C min^{-1}), followed by furnace cooling.

Cell assembly and testing

Full cells were sealed in an in-house made reactor using Aremco cerambond 552 sealant with oxygen electrode-side up. Silver mesh was used as the current collector with attached silver wires as leads. After assembly, the cell was heated up to 600 °C (heating rate 1 °C min^{-1}). When a temperature of 600 °C was reached, H_2 (flow rate 20 ml min^{-1}) was fed into the hydrogen electrode to reduce NiO to metallic Ni. When the reduction process was completed, a bubbler was connected between gas inlet of hydrogen electrode and inward gas to hydrolyse H_2 with 3% steam. EIS measurements were conducted at OCV conditions at 400–650 °C, with a frequency range from 10^5 to 0.1 Hz, an a.c. amplitude of 10 mV and zero d.c. bias. Electrochemical tests of PCFCs and PCECs were conducted individually by a Solartron 1400 electrochemical working station after a stable OCV was observed at the set temperature. Current density–voltage curves and current density–power density curves under fuel-cell mode were measured by a Solartron 1400 and 1470 electrochemical working station after a stable OCV was observed at the set temperature. Feedstock in the oxygen electrode was pure O_2. Feedstock in the hydrogen electrode was H_2 with 3% steam. Electrochemical data under fuel-cell mode were collected at a voltage range from OCV to 0.2 V at the set temperature. Continuous fuel-cell operation was conducted at a constant applied voltage of 0.75 V at 600 °C up to 200 h. Under electrolysis mode, the feedstock was pure H_2 (flow rate 20 ml min^{-1}) in the hydrogen electrode and O_2 with 30% steam in the oxygen electrode. Electrochemical tests were conducted after stable OCV was observed at the set temperature, at a voltage range from 1.5 V to OCV. Continuous electrolysis operation was conducted at a constant applied voltage of 1.4 V at 600 °C up to 200 h. PCFCs using CH_4 and C_2H_6 fuels were tested at 600 °C, using CH_4 or C_2H_6 (flow rate 20 ml min^{-1}) with 3% steam as the feedstock of the hydrogen electrode and pure oxygen (flow rate 60 ml min^{-1}) as the feedstock of the oxygen electrode. Leakage tests were conducted at 600 °C with the feedstock of pure hydrogen (flow rate 20 ml min^{-1}) for the hydrogen electrode and air (flow rate 60 ml min^{-1}) for the oxygen electrode.

Characterizations

X-ray diffraction measurements were conducted on a D8ADVANCE/Germany Bruker X-ray diffractometer using Ni-filter Cu Kα radiation (wavelength 0.154056 nm). Microstructures and EDS mapping were inspected under a scanning electron microscope (SEM) (JEOL 6700F). Surface chemistry was analysed by XPS using a Physical Electronics Versaprobe II X-ray Photoelectron Spectrometer. Surface roughness was inspected under AFM (Dimension Fastscan Atomic Force Microscope, Bruker) using a tapping mode. To measure the peeling strength of the oxygen electrode–electrolyte interface, double-sided tapes were attached to both sides of full cells in a rectangular shape (length 3 cm (1.18 inch), width 2.5 cm (1 inch)). The hydrogen electrode side was stuck to the testing bed with the oxygen electrode facing up and a scotch tape was next attached to the double-sided tape on the oxygen electrode side. During peeling tests, the oxygen electrode was peeled off from the electrolyte while the force was recorded and converted to peeling strength. Cross-sectional samples for STEM were prepared using a Thermo Fisher Helios 600 focused ion beam microscope/SEM. The samples were first coated with 10 nm of carbon using a Denton DV502A Evaporator to minimize the beam damage and charging effects. Additive protective layers included an e-beam-deposited Pt layer (100 nm) and an ion-beam-deposited carbon layer (1 μm). The samples were thinned step by step by lowering ion voltages from 30 to 2 kV and currents from 0.92 nA to 89 pA. The surface damage caused by the focused ion beam was removed by Ar^+ milling using a Fischione 1051 TEM Mill at room temperature with a voltage of 100 V and at an angle of 7°. The HAADF images and EDS mapping were taken on a Thermo Fisher Themis Z-STEM with an acceleration voltage of 200 kV.

Data availability

Data supporting the findings in the present work are available in the manuscript or Supplementary Information. Additional data are available from the corresponding authors upon reasonable request.

Acknowledgements This work is supported by the US Department of Energy (DoE), Office of Energy Efficiency and Renewable Energy, Hydrogen and Fuel Cell Technologies Office under DoE Idaho Operations Office under contract no. DE-AC07-05ID14517. Y.D. and J.L. acknowledge support by the DoE, Basic Energy Sciences, under award number DE-SC0002633 (Chemomechanics of Far-From-Equilibrium Interfaces). C.J. and M.Z. thank the subcontracts from Idaho National Laboratory and M.Z. also acknowledges funding support from National Science Foundation (no. OIA-2119688).

Author contributions W.B., W.W., Y.D., J.L. and D.D. conceived the project. W.B. and W.W. fabricated the cells and conducted electrochemical measurements. Y.D. conducted the theoretical analysis. Y.D. and W.B. analysed the data. B.W. contributed to STEM characterizations. W.T. contributed to cell fabrications and SEM characterizations. M.Z. contributed to AFM characterizations. C.J. contributed to peeling tests. H.D. contributed to the development of the oxygen electrode. W.F. contributed to XPS measurements. W.B., W.W., Y.D., J.L. and D.D. wrote the paper. All authors discussed and contributed to writing.

Competing interests The authors declare no competing interests.

Additional information

Supplementary information The online version contains supplementary material available at https://doi.org/10.1038/s41586-022-04457-y.

Correspondence and requests for materials should be addressed to Wei Wu, Yanhao Dong, Ju Li or Dong Ding.

Peer review information *Nature* thanks Truls Norby and the other, anonymous, reviewer(s) for their contribution to the peer review of this work.

nature portfolio

https://doi.org/10.1038/s41586-022-04457-y

Supplementary information

Revitalizing interface in protonic ceramic cells by acid etch

In the format provided by the authors and unedited

Supplementary information

Revitalizing interface in protonic ceramic cells by acid etch

Wenjuan Bian[1,2,†], Wei Wu[1,†,*], Baoming Wang[3], Wei Tang[1,2], Meng Zhou[2], Congrui Jin[4], Hanping Ding[1], Weiwei Fan[5], Yanhao Dong[5,*], Ju Li[3,5,*], Dong Ding[1,*]

[1]*Energy and Environmental Science and Technology, Idaho National Laboratory, Idaho Falls, ID 83415, USA*

[2]*Department of Chemical and Materials Engineering, New Mexico State University, Las Cruces, NM 88003, USA*

[3]*Department of Materials Science and Engineering, Massachusetts Institute of Technology, Cambridge, Massachusetts 02139, USA*

[4]*Department of Civil and Environmental Engineering, University of Nebraska–Lincoln, Lincoln, NE 68583, USA*

[5]*Department of Nuclear Science and Engineering, Massachusetts Institute of Technology, Cambridge, Massachusetts 02139, USA*

Table of contents

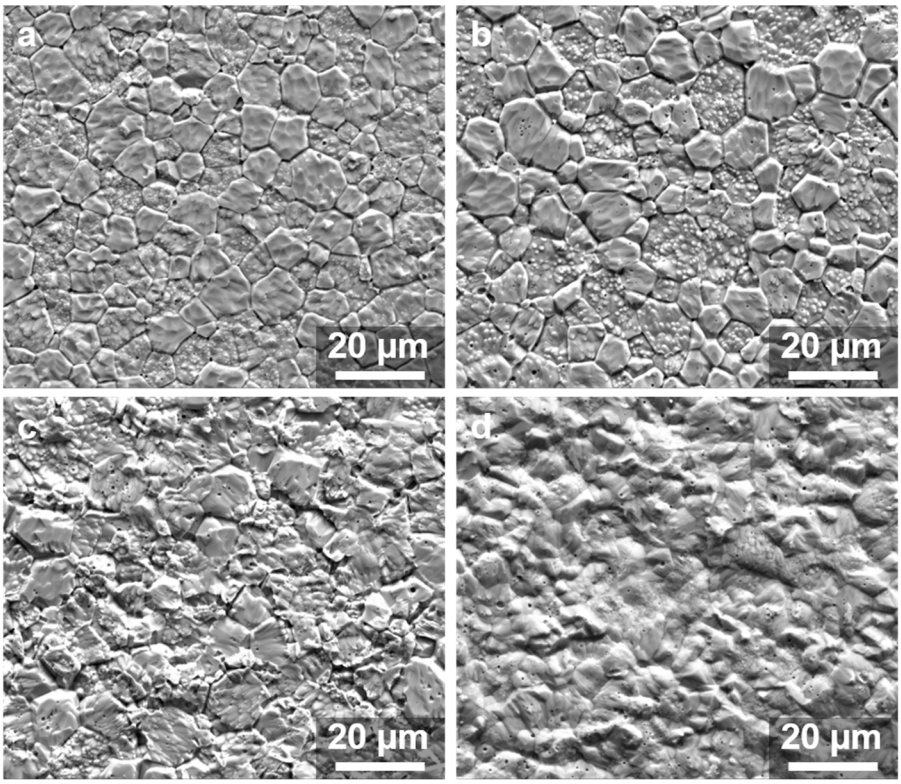

Supplementary Figure S1 Microstructure for 1 min (a), 2 min (b), 5 min (c) and 15 min (d) treated electrolyte surface of co-sintered hydrogen electrode-electrolyte bi-layer.

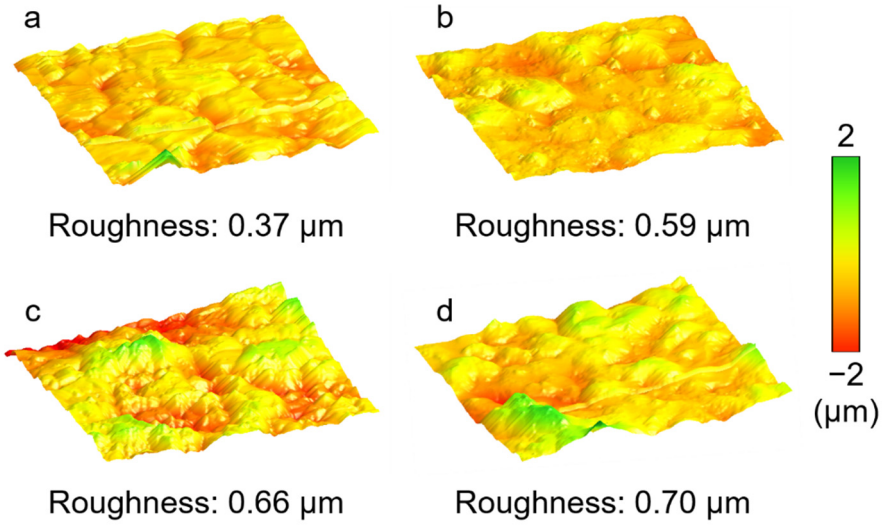

Supplementary Figure S2 AFM for 1 min (a), 2 min (b), 5 min (c) and 15 min (d) treated electrolyte surface of co-sintered hydrogen electrode-electrolyte bi-layer.

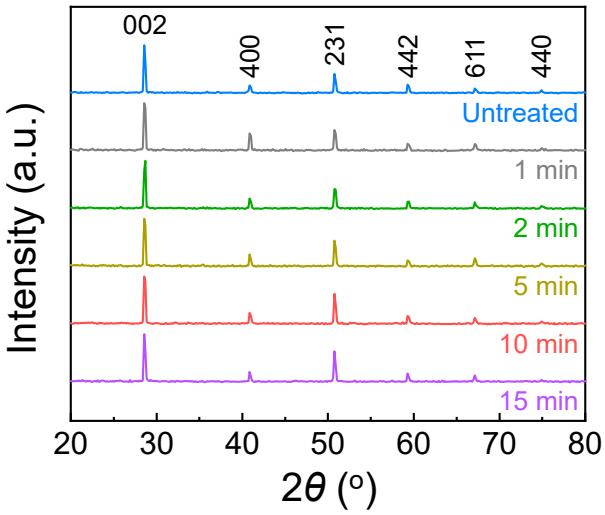

Supplementary Figure S3 XRD of differently treated electrolyte in the co-sintered hydrogen electrode-electrolyte bi-layer.

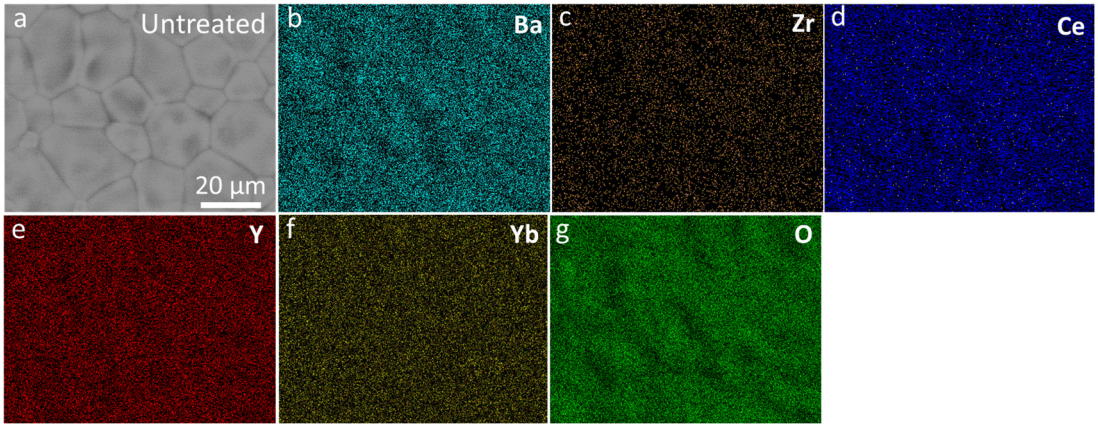

Supplementary Figure S4 SEM (a) and EDS mapping of (b) Ba, (c) Zr, (d) Ce, (e) Y, (f) Yb, and (g) O at the surface of the untreated electrolyte surface of the co-sintered hydrogen electrode-electrolyte bi-layer.

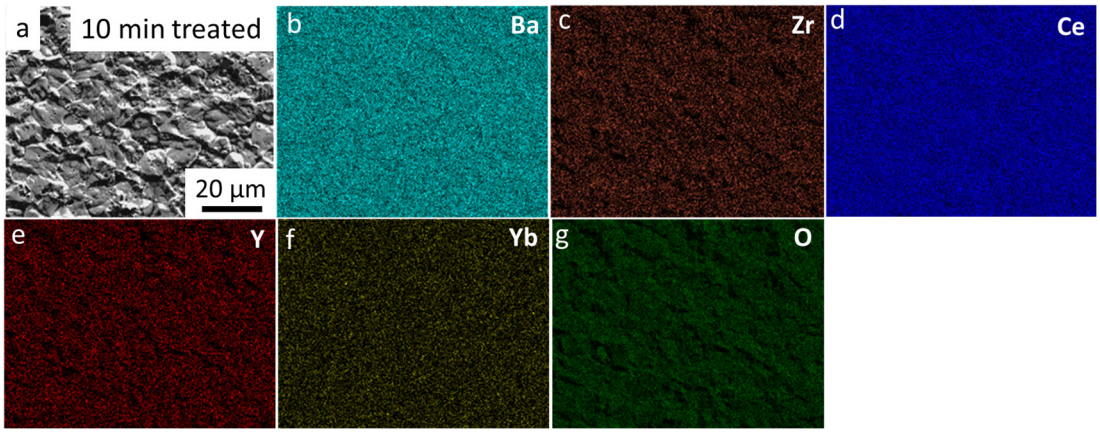

Supplementary Figure S5 SEM (a) and EDS mapping of (b) Ba, (c) Zr, (d) Ce, (e) Y, (f) Yb, and (g) O at the surface of the 10 min treated electrolyte surface of the co-sintered hydrogen electrode-electrolyte bi-layer.

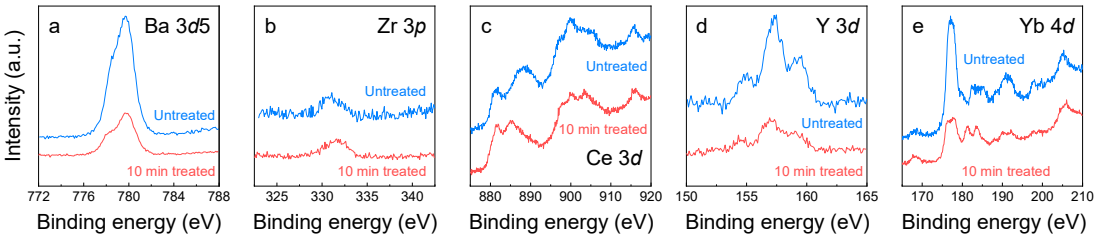

Supplementary Figure S6 XPS spectra of (a) Ba 3*d*5, (b) Zr 3*p*, (c) Ce 3*d*, (d) Y 3*d*, and (e) Yb 4*d* peaks of the untreated (top, in blue) and 10 min treated (bottom, in red) electrolyte surfaces of the co-sintered hydrogen electrode-electrolyte bi-layer.

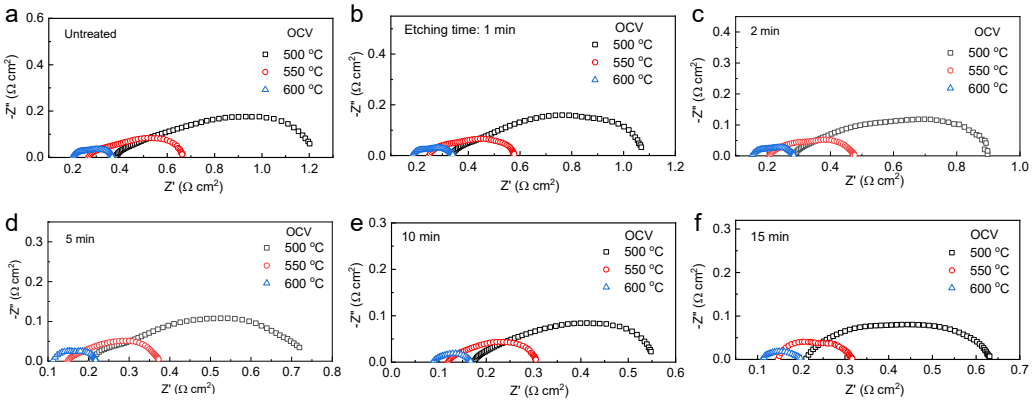

Supplementary Figure S7 EIS for untreated (a), and 1 min (b), 2 min (c), 5 min (d), 10 min (e) and 15 min (f) treated cells at OCV condition at 500, 550, and 600 ºC.

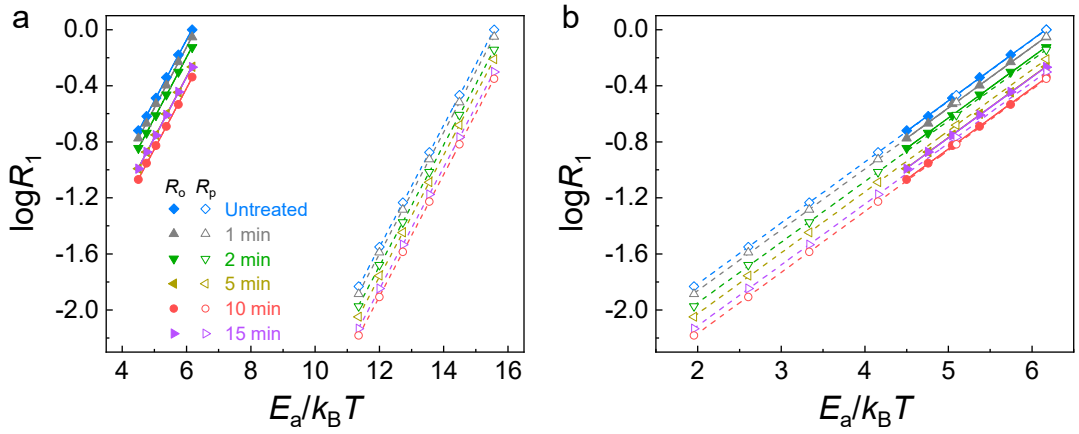

Supplementary Figure S8 Normalization process for **Figure 3f**. Starting from **Figure 3b** and **3c**, we first normalized their *y*-axis R_o by the corresponding data R_o^0 in the untreated cell and R_p by the corresponding data R_p^0 in the untreated cell to obtain R_1 (i.e., R_o/R_o^0 for the ohmic part and R_p/R_p^0 for the polarization part), and normalized their *x*-axis $1/T$ by the corresponding activation energy $E_{a,o}/k_B$ or $E_{a,p}/k_B$ to obtain E_a/k_BT. This first step gives (a). Then we left-shifted the curves for the polarization part to superimpose R_1 of R_o and R_p in the untreated cell (blue data points) at the lowest T=400 °C. This second step gives (b). Lastly, we divided R_1 of both R_o and R_p by A_o^0/A_o to obtain R. This final step gives **Figure 3f**.

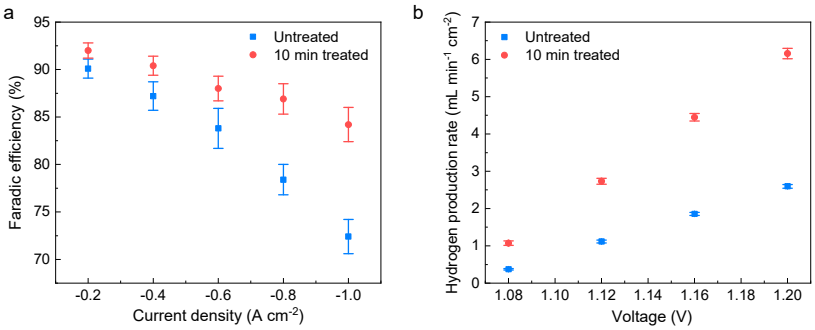

Supplementary Figure S9 (a) Faradic efficiency of the untreated and the 10 min treated cells at a function of current density under PCEC operation mode at 600 ºC. (b) Hydrogen production rate of the untreated and the 10 min treated cells at a function of applied voltage under PCEC operation mode at 600 ºC.

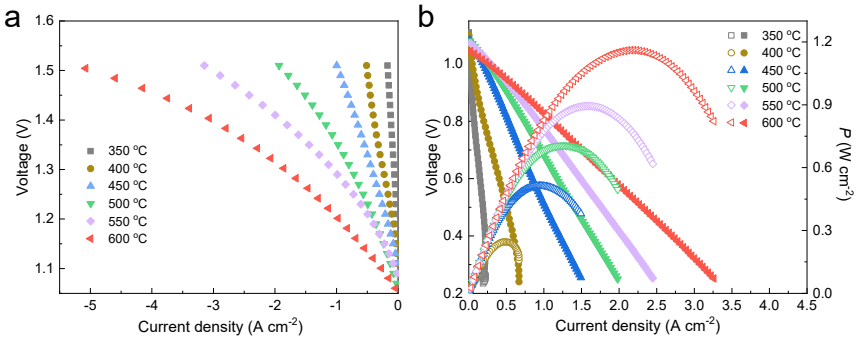

Supplementary Figure S10 PCEC (a) and PCFC (b) performances of 10 min treated cells at 350, 400, 450, 500, 550 and 600 ºC.

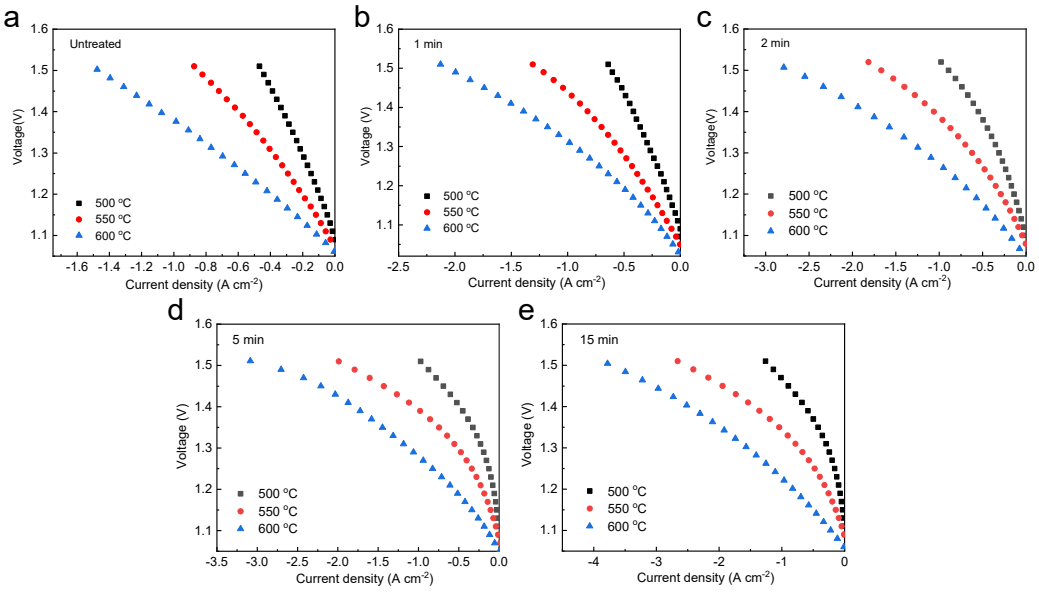

Supplementary Figure S11 PCEC performances of untreated (a), and 1 min (b), 2 min (c), 5 min (d), and 15 min (e) treated cells at 500, 550, and 600 °C.

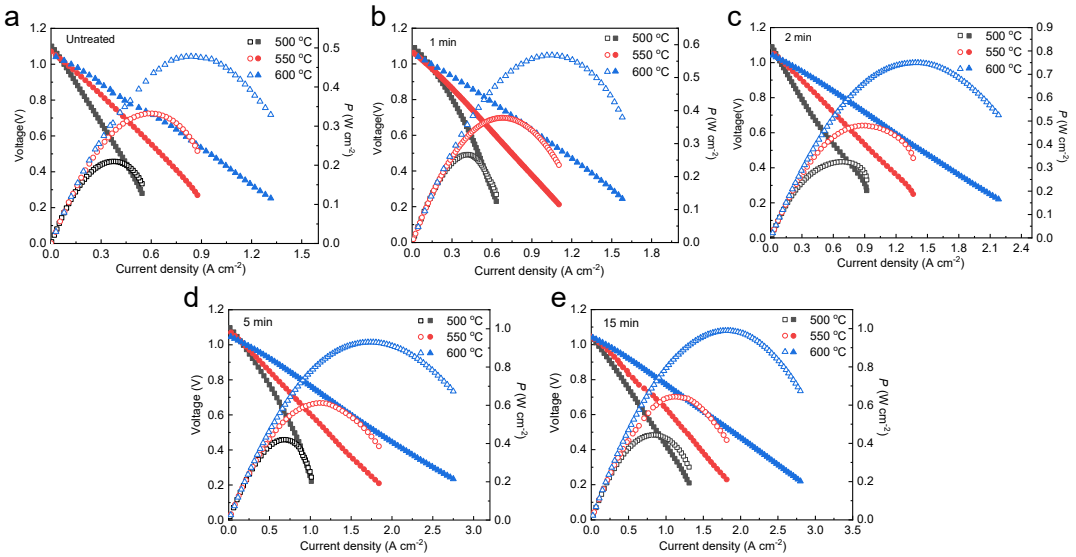

Supplementary Figure S12 PCFC performances of untreated (a), and 1 min (b), 2 min (c), 5 min (d), and 15 min (e) treated cells at 500, 550, and 600 °C.

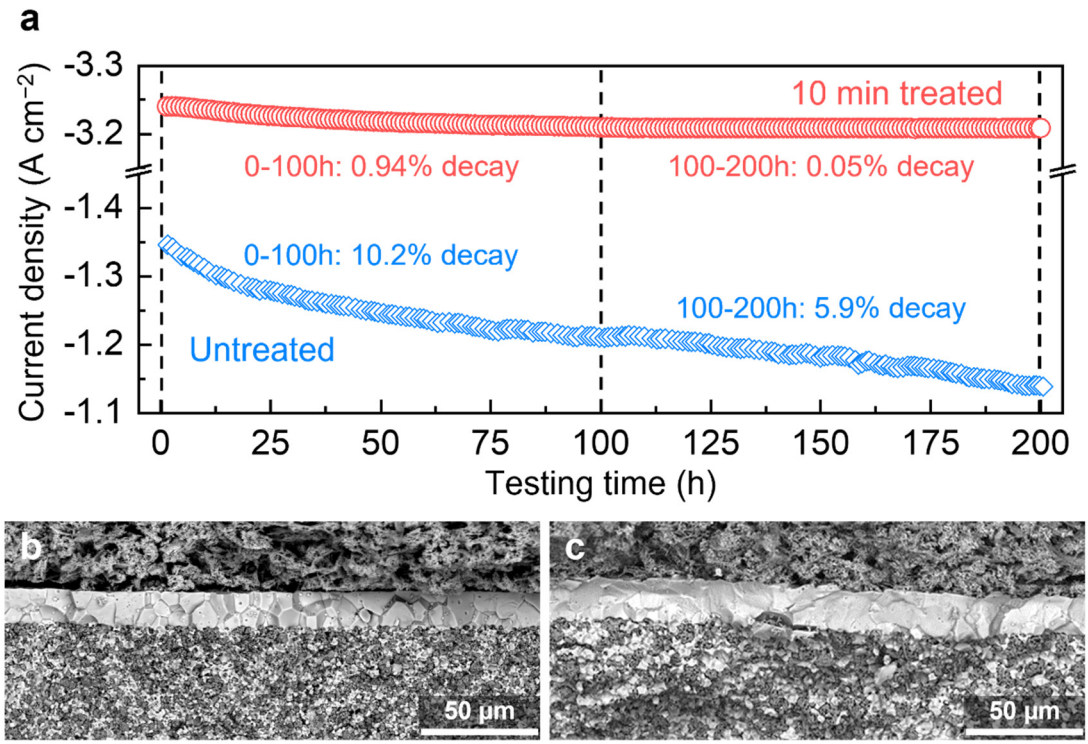

Supplementary Figure S13 (a) Current density curves of untreated and 10 min treated cells under PCEC operation at 1.4 V at 600 ºC with 30% steam in oxygen electrode. Fracture surface of untreated (b) and 10 min treated (c) cells after 200 h testing in (a). Cells made up of 22 μm thick BZCYYb electrolyte and PNC55 oxygen electrode and with different etching treatment conditions. In SOEC, high-pressure oxygen bubbles due to internal chemical reaction were observed at grain boundaries of zirconia electrolytes close to the oxygen electrode, which preferentially nucleate and grow at blocking transverse grain boundaries perpendicular to the electric field direction. At this stage, it is not clear how the change of charge carrier from oxygen ions to protons would affect the precipitated grain-boundary gaseous species in PCEC electrolytes. Future work is required to identify the existence and trapped species of the hypothesized grain boundary bubbles.

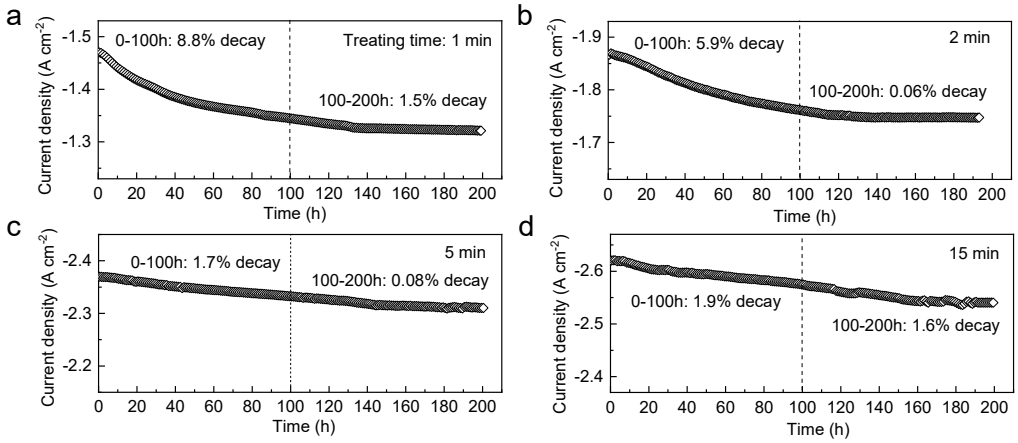

Supplementary Figure S14 Current density curves of 1 min (a), 2 min (b), 5 min (c), and 15 min (d) treated cells under PCEC operation at 1.4 V at 600 ºC.

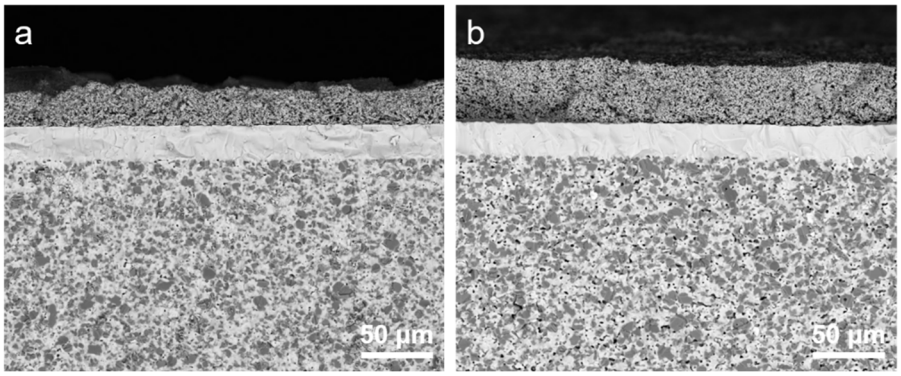

Supplementary Figure S15 Fracture surface of untreated (a) and 10 min treated (b) cells before PCEC testing.

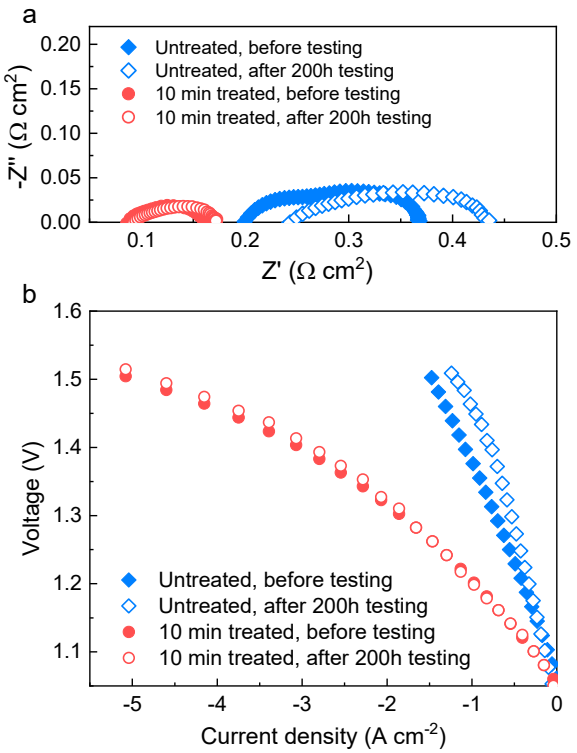

Supplementary Figure S16 (a) EIS at OCV and (b) polarization curves at 600 ºC of the untreated and the 10 min treated cells before and after the 200 h PCEC testing in **Supplementary Figure S13a**.

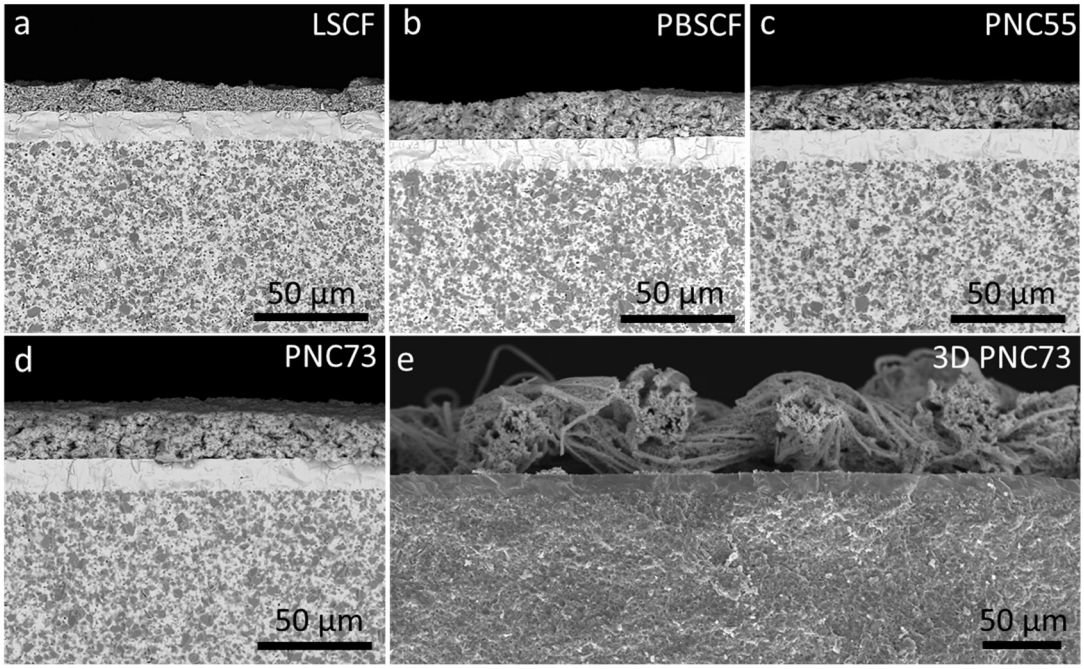

Supplementary Figure S17 Fracture surface of 10 min treated cells made up of 16 µm BZCYYb electrolyte and LSCF (a), PBSCF (b), PNC55 (c), PNC73 (d), and 3D PNC73 (e) oxygen electrode.

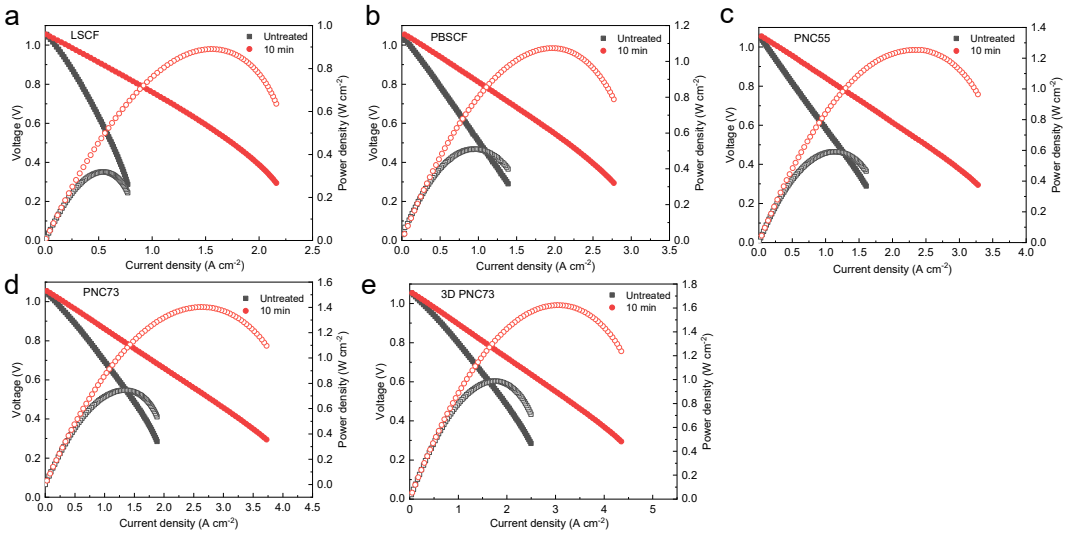

Supplementary Figure S18 PCFC performances (at 600 ºC) of untreated (in black) and 10 min treated (in red) cells made up of 16 µm BZCYYb electrolyte and LSCF (a), PBSCF (b), PNC55 (c), PNC73 (d), and 3D PNC73 (e) oxygen electrode.

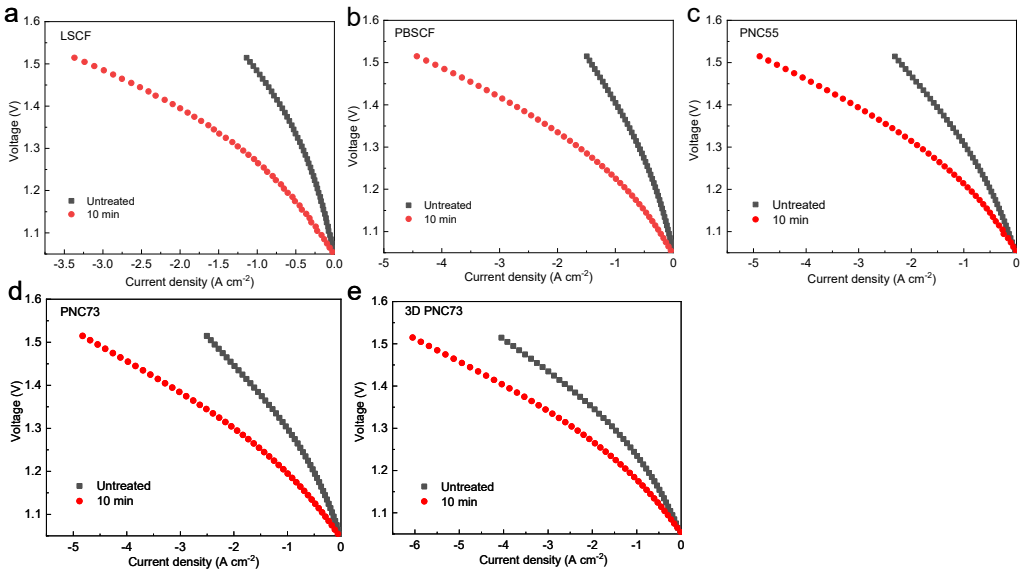

Supplementary Figure S19 PCEC performances (at 600 ºC) of untreated (in black) and 10 min treated (in red) cells made up of 16 µm BZCYYb electrolyte and LSCF (a), PBSCF (b), PNC55 (c), PNC73 (d), and 3D PNC73 (e) oxygen electrode.

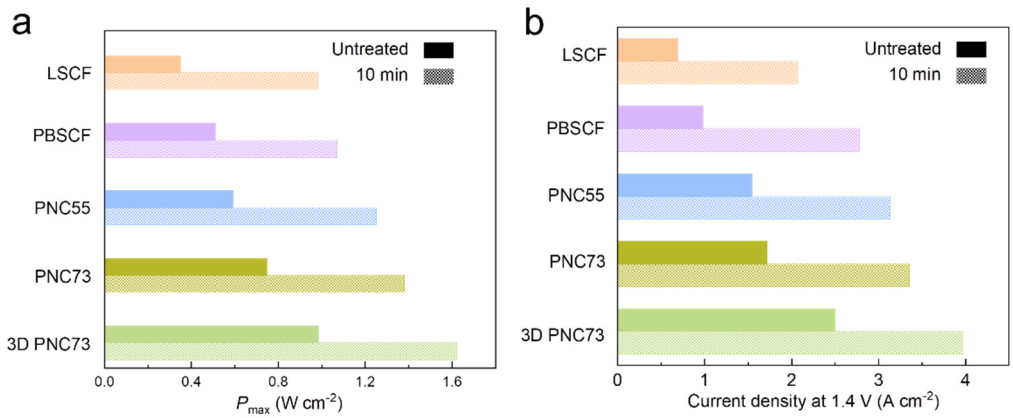

Supplementary Figure S20 Comparisons of the PCFC peak power density P_{max} (a) and the PCEC current density at 1.4 V applied voltage (b) between untreated and 10 min treated cells made up of 16 μm BZCYYb electrolyte and LSCF, PBSCF, PNC55, PNC73, and 3D PNC73 oxygen electrode at 600 ºC.

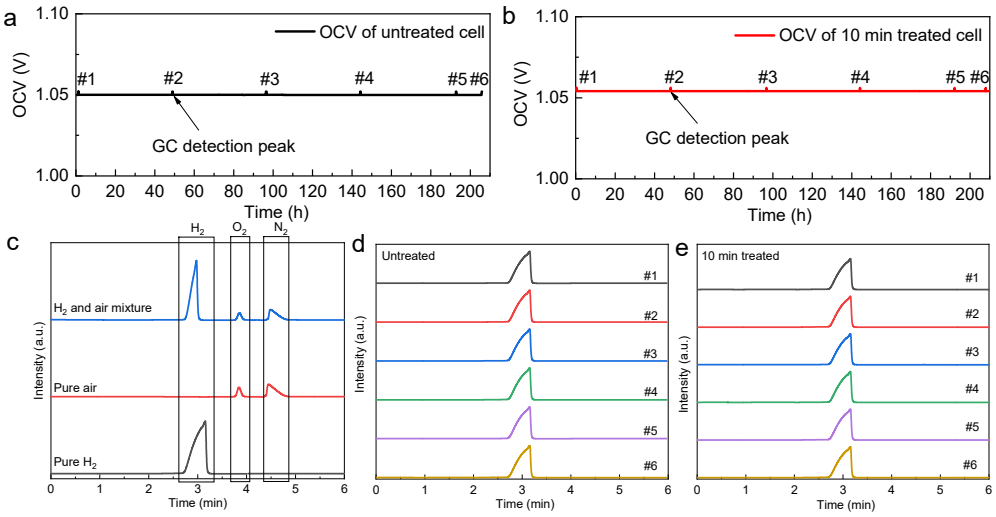

Supplementary Figure S21 Leakage tests of untreated (a) and 10 min treated (b) cells made up of 16 μm BZCYYb electrolyte and PNC55 oxygen electrode at 600 ºC. Open circuit voltage (OCV) was monitored continuously for 205 h with the feedstock of H_2 in the fuel electrode and air in the oxygen electrode. Gas chromatography was conducted to detect the gas condition in fuel electrode every 48 hours for 5 times (peak #1 to #5) and at the end of the test at 205 h (peak #6), which slightly affects the OCV values in (a, b) due to equipment crosstalk. Gas chromatography for three reference gases (pure H_2, pure air, and H_2+air mixture) was first conducted in (c), which shows H_2 detection peak at 2.9 min, O_2 detection peak at 3.9 min, and N_2 detection peak at 4.7 min after the starting time of the gas chromatography. Gas chromatography for the untreated (d) and 10 min treated (e) cells shows H_2 detection peak at 2.9 min (after the starting time of the gas chromatography) and no O_2 or N_2 peaks. The results indicate the cells are gas-tight with dense electrolyte and good sealing and without gas leakage.

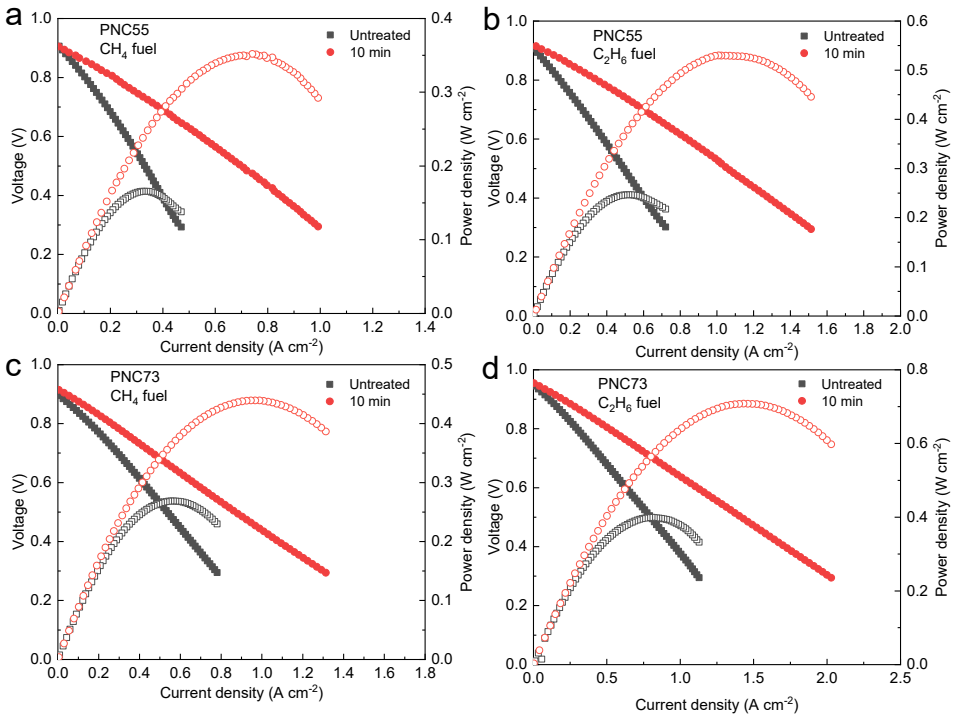

Supplementary Figure S22 PCFC performances (at 600 ºC) of untreated (in black) and 10 min treated (in red) using (a, c) CH_4 and (b, d) C_2H_6 fuel. Cells made up of 16 µm BZCYYb electrolyte and PNC55 (a, b), and PNC73 (c, d) oxygen electrode.

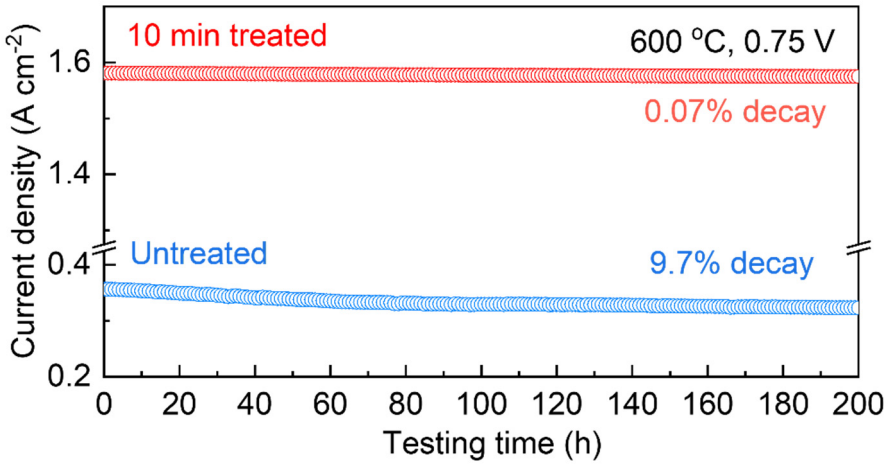

Supplementary Figure S23 Current density curves of untreated and 10 min treated cells under PCFC operation at 0.75 V at 600 °C. Cells made up of 16 μm BZCYYb electrolyte and PNC73 oxygen electrode. Feedstock is 97% H_2+3% H_2O (flow rate: 20 mL/min) in fuel electrode and O_2 (flow rate: 60 mL/min) in oxygen electrode. Initial current density: 0.36 A cm^{-2} for untreated cell and 1.58 A cm^{-2} of 10 min treated cell. The 10 min treated cell shows 0.07% decay in current density over 200 h continuous PCFC operation, compared to 9.7% decay for the untreated cell.

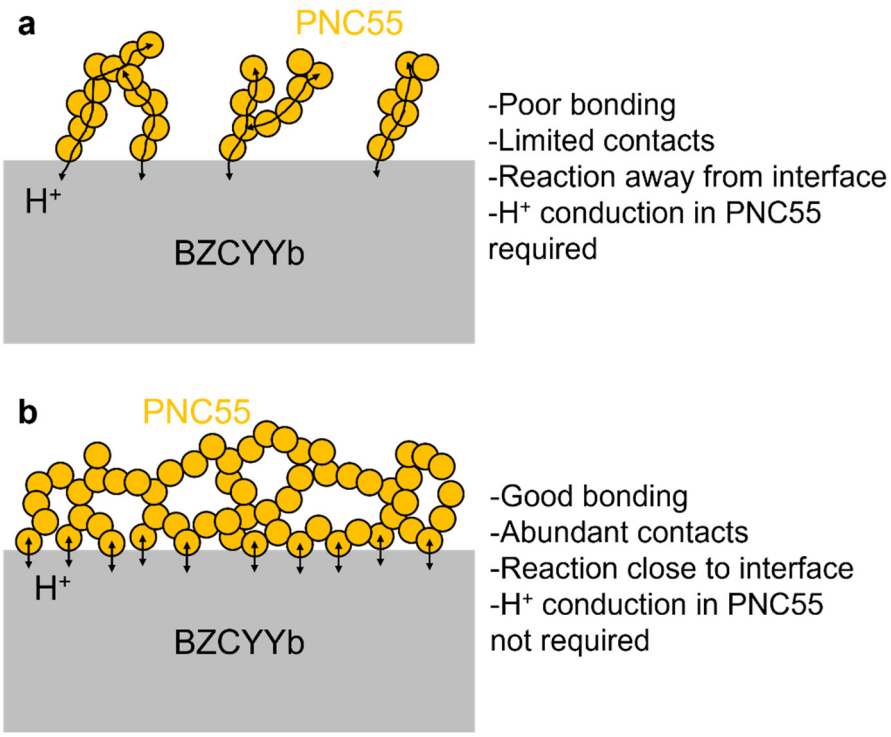

Supplementary Figure S24 Schematics comparing the reaction mechanisms of poorly (a) vs. well (b) bonded PNC55 on BZCYYb near the oxygen electrode-electrolyte interface. The acid treatment offers a way to obtain good bonding, and the resultant rough interface was not plotted in the schematics for simplicity.

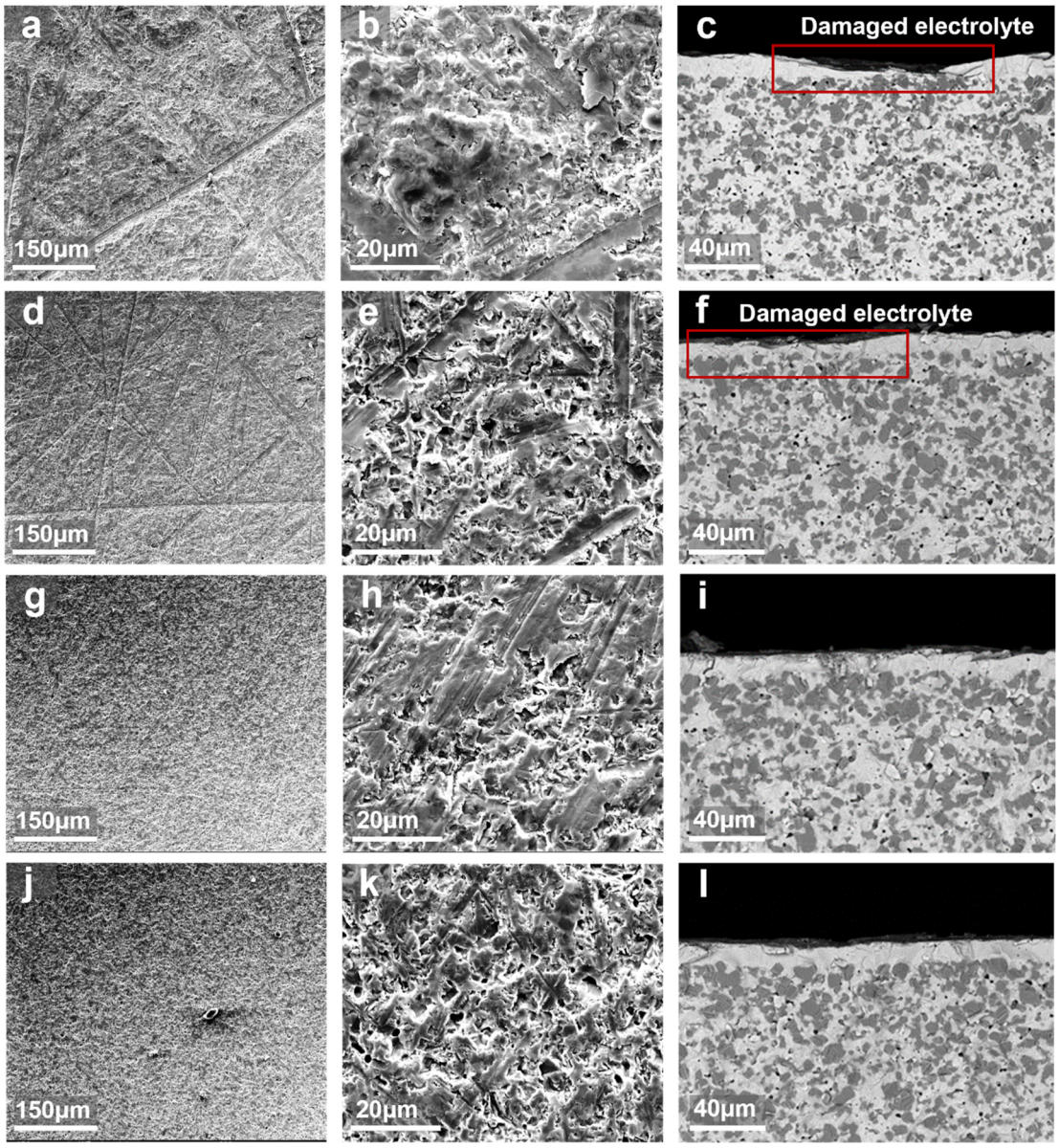

Supplementary Figure S25 SEM of the top surface (a,b,d,e,g,h,j,k) and the cross-section (c,f,i,l) of the half cells mechanically polished by 80 (a-c), 200 (d-f), 400 (g-i), and 800 (j-l) grit SiC sandpapers. Damaged electrolytes can be clearly seen from the cross-section images in (c) and (f).

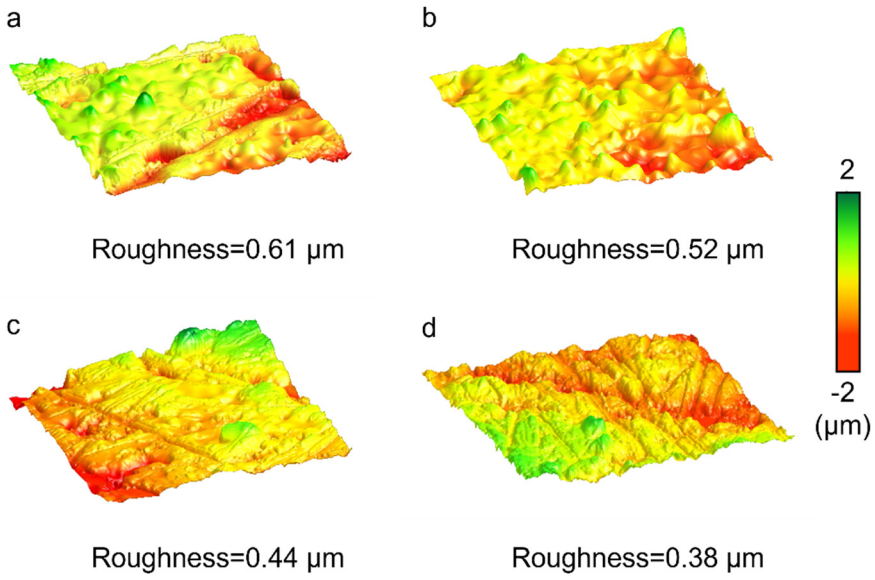

Supplementary Figure S26 AFM of the electrolyte surface and the measured surface roughness of the half cells mechanically polished by 80 (a), 200 (b), 400 (c), and 800 (d) grit SiC sandpapers.

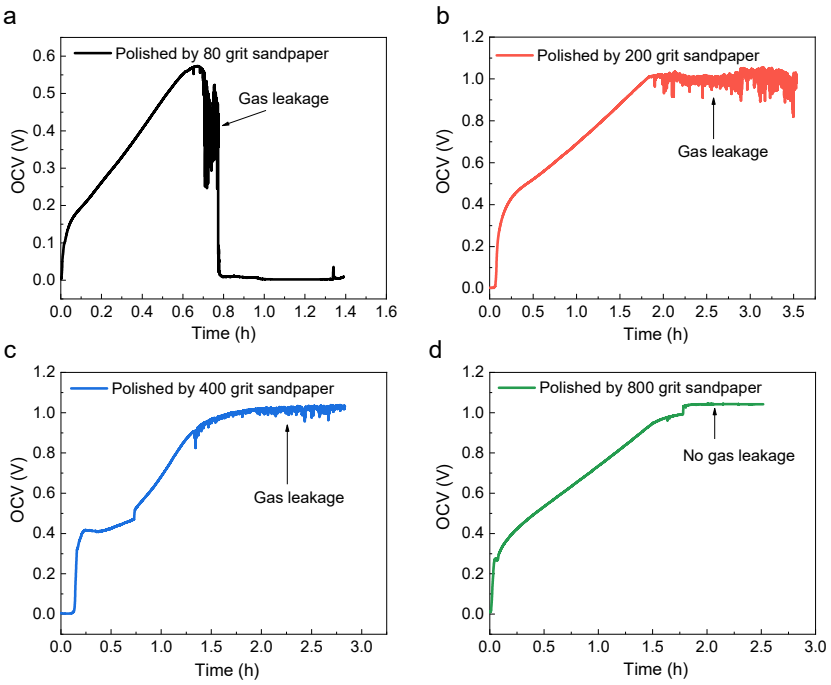

Supplementary Figure S27 Measured open circuit voltage (OCV) of the full cells polished by 80 (a), 200 (b), 400 (c), and 800 (d) grit sandpapers during NiO reduction at 600 ºC. Decreased or fluctuated OCV was observed in (a-c), indicating gas leakage. The reduction process was conducted in two steps: (1) 15% H_2 with 85% Ar (total flow rate: 20 mL min^{-1}) was fed into the fuel electrode, and O_2 (flow rate: 20 mL min^{-1}) was fed into the oxygen electrode. (2) After OCV reached a stable value, pure H_2 (flow rate: 20 mL min^{-1}) was fed into the fuel electrode for further reduction, and O_2 (flow rate: 60 mL min^{-1}) were fed into the oxygen electrode.

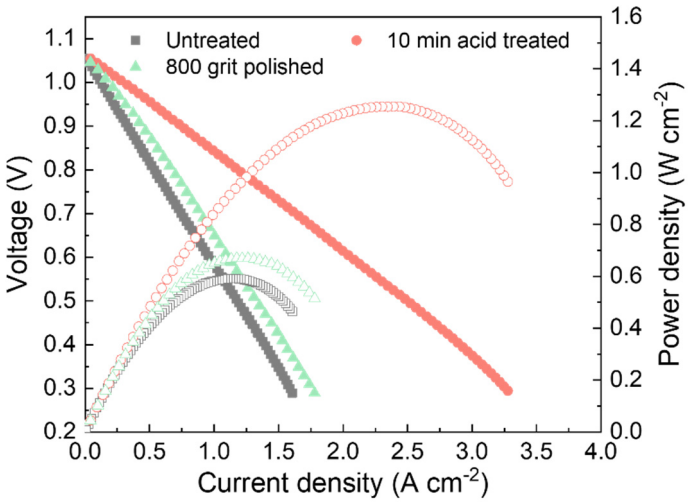

Supplementary Figure S28 Comparison of the PCFC performance at 600 ºC for the untreated, 10 min acid treated, and 800 grid sandpaper polished cells.

Supplementary Table S1 Peeling strength of the oxygen electrode (PNC55)-electrolyte interface of differently treated cells.

	Untreated	Treating time (min)				
		1	2	5	10	15
Peeling strength (N)	18.6	18.8	19.9	22	23.5	20.2

Supplementary Table S2 Chemical compositions from EDS mapping on the electrolyte surface of the untreated and 10 min treated half cells. Note EDS is a semi-quantitative measurement of the chemical compositions and have a micron-scale detection depth.

	Atomic percentage (%)					
	Ba	Zr	Ce	Y	Yb	O
Untreated	27.8	2.6	18.0	2.2	2.6	46.7
10 min treated	28.4	2.4	18.5	2.3	2.6	45.8

Supplementary Table S3 Cation compositions from EDS mapping on the electrolyte surface of the untreated and 10 min treated half cells. Theoretical cation composition for BZCYYb is also listed for comparison.

	Atomic ratio over (Zr+Ce+Y+Yb)				
	Ba	Zr	Ce	Y	Yb
Untreated	1.09	0.10	0.71	0.09	0.10
10 min treated	1.10	0.09	0.72	0.09	0.10
BZCYYb	1.00	0.10	0.70	0.10	0.10

Supplementary Table S4 Cation compositions on BZCYYb surface of the untreated and 10 min treated half cells from XPS measurements. Note XPS is a semi-quantitative measurement of the surface chemical compositions and have a nm-scale detection depth.

	Atomic ratio over (Zr+Ce+Y+Yb)				
	Ba	Zr	Ce	Y	Yb
Untreated	0.89	0.07	0.74	0.15	0.04
10 min treated	0.47	0.07	0.78	0.10	0.04

Supplementary Table S5 Fitting details of R_o and R_p in the Arrhenius form in Eq. (1,2).

	Untreated	Treating time (min)					Bulk electrolyte
		1	2	5	10	15	
A_o (Ω cm^2)	1.24	1.40	1.65	2.29	2.77	2.19	2.91
$E_{a,o}$ (eV)	0.358	0.358	0.357	0.358	0.357	0.357	0.359
Error of $E_{a,o}$ (eV)	0.003	0.003	0.002	0.003	0.003	0.003	0.003
r^2 of R_o fitting	0.99976	0.99967	0.99981	0.99974	0.9998	0.99978	0.99976
A_p (10^{-7} Ω cm^2)	11.3	9.95	8.33	6.67	4.79	5.60	/
$E_{a,p}$ (eV)	0.904	0.902	0.900	0.904	0.905	0.902	/
Error of $E_{a,p}$ (eV)	0.0002	0.002	0.003	0.002	0.002	0.001	/
r^2 of R_p fitting	0.99997	0.99996	0.99996	0.99997	0.99998	0.99999	/

Supplementary Table S6 Comparison of ohmic resistance R_o and polarization resistance R_p (calculated from EIS data in **Figure S15a**) for the untreated and the 10 min treated cells before and after the 200 h PCEC testing in **Figure 5a**.

	R_o (Ω cm^2)	R_p (Ω cm^2)
Untreated cell before testing	0.20	0.17
Untreated cell after 200 h PCEC testing	0.24	0.19
10 min treated cell before testing	0.09	0.07
10 min treated cell after 200 h PCEC testing	0.09	0.08

Supplementary Table S7 PCFC peak power density for untreated (denoted as "Un-") and 10 min treated (denoted as "Tr-") cells made up of 16 μm thick BZCYYb electrolyte and different oxygen electrodes (specified in the table).

Operation temperature (°C)	Peak power density with different oxygen electrode (mW cm^{-2})									
	LSCF		PBSCF		PNC55		PNC73		3D PNC73	
	Un-	Tr-	Un-	Tr-	Un-	Tr-	Un-	Tr-	Un-	Tr-
600	350	980	510	1071	592	1250	747	1379	983	1620
550	165	721	264	801	324	912	458	982	610	1252
500	76	447	134	517	162	634	276	691	389	901
450	/	254	/	332	/	400	128	456	176	651
400	/	137	/	180	/	221	/	282	89	474
350	/	77	/	90	/	120	/	150	/	288

Supplementary Table S8 Fuel efficiencies of untreated and differently treated cells made up of 16 μm thick BZCYYb electrolyte and PNC55, PNC73, and 3D PNC73 oxygen electrodes at 600 ºC. The feedstock is 97% H_2+3% H_2O (H_2 flow rate: 20 mL/min) for hydrogen electrode and O_2 (flow rate: 60 mL/min) for oxygen electrode.

Treatment condition	Fuel efficiency with different oxygen electrode (%)		
	PNC55	PNC73	3D PNC73
Untreated	100	98	99
1 min treated	98	99	100
2 min treated	99	100	98
5 min treated	100	99	99
10 min treated	98	98	100
15 min treated	99	99	98